

UNFOLDING A TANGENT EQUILIBRIUM-TO-PERIODIC HETEROCLINIC CYCLE

ALAN R. CHAMPNEYS ^{*}, VIVIEN KIRK [†], EDGAR KNOBLOCH [‡], BART E.
OLDEMAN [§], AND J.D.M. RADEMACHER [¶]

May 6, 2009

Abstract. The dynamics occurring near a heteroclinic cycle between a hyperbolic equilibrium and a hyperbolic periodic orbit is analyzed. The case of interest is when the equilibrium has a one-dimensional unstable manifold and a two-dimensional stable manifold while the stable and unstable manifolds of the periodic orbit are both two-dimensional. A codimension-two heteroclinic cycle occurs when there are two codimension-one heteroclinic connections, with the connection from the periodic orbit to the equilibrium corresponding to a tangency between the two relevant manifolds. The results are restricted to \mathbb{R}^3 , the lowest possible dimension in which such a heteroclinic cycle can occur, but are expected to be applicable to systems of higher dimension as well.

A geometric analysis is used to partially unfold the dynamics near such a heteroclinic cycle by constructing a leading-order expression for the Poincaré map in a full neighbourhood of the cycle in both phase and parameter space. Curves of orbits homoclinic to the equilibrium are located in a generic parameter plane, as are curves of homoclinic tangencies to the periodic orbit. Moreover, it is shown how curves of folds of periodic orbits, which have different asymptotics near the homoclinic bifurcation of the equilibrium and the homoclinic bifurcation of the periodic orbit, are glued together near the codimension-two point.

A simple global assumption is made about the existence of a pair of codimension-two heteroclinic cycles corresponding to a first and last tangency of the stable manifold of the equilibrium and the unstable manifold of the periodic orbit. Under this assumption, it is shown how the locus of homoclinic orbits to the equilibrium should oscillate in the parameter space, a phenomenon known as *homoclinic snaking*. Finally, we present several numerical examples of systems that arise in applications, which corroborate and illustrate our theory.

Key words: global bifurcation, Shil'nikov analysis, heteroclinic cycle, homoclinic orbit, homoclinic tangency, snaking.

AMS subject classifications: 34C23, 34C37, 37C29, 37G20.

1. Introduction. We are interested in the dynamics near a heteroclinic cycle connecting a hyperbolic equilibrium solution and a hyperbolic periodic orbit, referred to here as an *EP-cycle*. Specifically, we consider dynamics in \mathbb{R}^3 , and assume that the equilibrium (denoted E) has a one-dimensional unstable manifold $W^u(E)$, while the periodic orbit (denoted P) has a two-dimensional unstable manifold $W^u(P)$. In this case, a heteroclinic connection from E to P generically will be of codimension one, while a connection from P to E generically will be of codimension zero. We denote by *EP1-cycle* an EP-cycle in \mathbb{R}^3 where the connections from E to P and from P to E are both of the appropriate generic type. Such a heteroclinic cycle as a whole is then a codimension-one object, i.e., it occurs at isolated points in a generic one-parameter family of vector fields. In a two-parameter setting, EP1-cycles will occur on one-dimensional curves in the two-parameter space, with one possible endpoint of a curve of EP1-cycles occurring when a tangency develops between $W^u(P)$ and $W^s(E)$; we shall refer to such a codimension-two cycle as an *EP1t-cycle*, and call the point in a two-parameter space at which an EP1t-cycle exists an *EP1t-point*.

^{*}Department of Engineering Mathematics, University of Bristol, Bristol BS8 1TR, UK

[†]Department of Mathematics, University of Auckland, Private Bag 92019, Auckland, NZ

[‡]Department of Physics, University of California, Berkeley CA94720, USA

[§]Computer Science and Software Engineering, Concordia University, 1455 de Maisonneuve Blvd. W., Montreal, QC, H3G 1M8, Canada

[¶]Department MAS, Centre for Mathematics and Computer Science (CWI), Science Park 123, 1098 XG Amsterdam, The Netherlands

EP1t-points arise in a number of applications. For instance, Champneys *et al.* [4] study ways in which branches of isolated travelling pulses interact with small-amplitude waves born in a Hopf bifurcation, in the context of excitable systems. By passing to a moving frame of reference, they reduce this question to the study of various codimension-two mechanisms for the termination of curves of homoclinic bifurcations as a Hopf bifurcation is approached. In two of the models discussed in that paper, i.e., the FitzHugh-Nagumo equations and a nine-dimensional model of intracellular calcium dynamics, it is found that an EP1t-point acts as an organising centre for homoclinic bifurcations of equilibria. In the parameter plane of the FitzHugh-Nagumo model many different branches of homoclinic orbits appear to have single folds near an EP1t-point, while in the calcium model a single branch of homoclinic orbits folds many times (in a “homoclinic snake”) near a pair of EP1t-points. EP1t-points have also been seen in a three-dimensional model motivated by studies of semiconductor lasers with optical reinjection [20]. In this case, folds of a single curve of homoclinic orbits again accumulate on a pair of EP1t-points, in a manner similar to that seen in the nine-dimensional calcium model in [4]. The theoretical study of EP1t-points presented here is motivated by our desire to explain the observed folding and accumulation of homoclinic bifurcation curves in these and other systems.

Our main aim in this paper is to provide a geometric analysis that unfolds the dynamics near an EP1t-cycle. We are interested in how curves of codimension-one homoclinic bifurcations in a suitable parameter plane emanate from an EP1t-point. Specifically, we locate curves of homoclinic tangencies to the periodic orbit (which we call P -homoclinic tangencies, with non-tangent homoclinic orbits being called P -homoclinics) and homoclinic orbits to the equilibrium (E -homoclinics). We also investigate bifurcations of periodic orbits near EP1t-points. Curves of folds of periodic orbits in a parameter plane are known to exist with different asymptotics near P -homoclinic tangencies and E -homoclinics (see, for example, [13, 10]); we explain how such curves are glued together near an EP1t-point. Motivated by several examples of snaking curves of E -homoclinic orbits observed in applications, we explain geometrically how such behaviour can arise when there is a curve (in two-parameter space) of EP1-cycles, whose extrema are EP1t-points. Such a geometry would occur when the two-dimensional manifolds $W^u(P)$ and $W^s(E)$ are “pulled through” each other as we vary a second parameter. Finally, we present several numerical examples of systems that arise in the applications discussed in the previous paragraph, which corroborate and illustrate our theory.

Our method of analysis follows a standard procedure. We first construct a model of the dynamics near an EP1t-cycle in terms of Poincaré maps between neighbourhoods of E and P , and then analyze the ensuing algebraic bifurcation equations. Near each of E and P we derive local maps by assuming that the flow is governed by appropriate linearised vector fields in these regions. The flow near the heteroclinic connections between E and P is approximated by linearising about each heteroclinic connection, which enables us to derive two global maps. Appropriate composition of the local and global maps yields the desired return maps. While we do not give complete proofs that this model approximates the dynamics near the heteroclinic cycle, we believe a rigorous proof is possible, for instance by way of the methods described in [29, 30]. Our aim instead is to provide a direct and intuitive geometric picture and to uncover the scaling laws of the separate codimension-one bifurcations that occur near the codimension-two point.

In this paper we restrict to the lowest possible phase space dimension, namely

\mathbb{R}^3 , capable of supporting an EP1t-point. However, the results we obtain are likely to apply to systems in higher dimensions where the equilibrium and periodic orbit have additional strongly stable directions. Results such as the so-called homoclinic centre manifold theorem [22, 32, 37], or Lin’s method for EP-cycles [28, 29, 30] may well provide the required extension to higher dimensions.

There are a number of previous theoretical studies on EP cycles (also called singular cycles) from an ergodic theory point of view, focusing on properties of non-wandering sets (see [1, 23, 24, 26] and references therein). Such properties were studied for EP1t cycles in [25] when the eigenvalues at E are real with a stable leading eigenvalue, and the Floquet multipliers at P are positive. Our results for this case are complementary, providing details on parameter curves for certain specific solutions, as described in §2 and §3. Moreover, we also study the case where the leading eigenvalue at E is unstable, as well as complex eigenvalues at E and negative Floquet multipliers at P .

The outline of the paper is as follows. §2 contains a summary of our main findings about the bifurcations seen near an EP1t-point. Details about construction of the return maps and results on the organisation of P - and E -homoclinic orbits near an EP1t-point are contained in §§3–5. §6 contains results on the dynamics of the complete return map near an EP1t-cycle, specifically on the locations of folds of periodic orbits. §7 considers the more global analysis which motivates the snaking bifurcation diagrams. §8 contains numerical results on example systems, and finally, §9 draws conclusions and suggests avenues for future work.

2. Approach and main results. We use a standard method of analysis to unfold an EP1t-point. That is, we define appropriate Poincaré sections close to E and P in order to reduce the dynamics nearby (in phase and parameter space) to the composition of various local and global maps, as shown in Fig. 3.1. Once the maps are constructed, we use them to determine the location in parameter space of *single-pulse* E -homoclinic orbits and P -homoclinic tangencies, as well as folds of *primary* periodic orbits. By single-pulse we mean E -homoclinics that do not come close to E other than as $t \rightarrow \pm\infty$, although they may visit arbitrarily close to P ; single-pulse P -homoclinics visit a neighbourhood of P only as $t \rightarrow \pm\infty$. By primary periodic orbits we mean those that form a sequence converging to a single-pulse E -homoclinic or P -homoclinic tangency. On the level of these maps our analytical results are rigorous except for the loci of folds of periodic orbits for complex eigenvalues at E .

Since locating single-pulse E -homoclinics involves tracking only the unstable manifold of E , the dynamics in a neighbourhood of E will not affect the loci of E -homoclinics in parameter space. Similarly, the dynamics near P will not affect the parametric curves of P -homoclinic tangencies. Thus, for the purposes of finding single-pulse E -homoclinics and P -homoclinic tangencies we need to consider only three cases. Case I, where the eigenvalues of E are real and the Floquet multipliers of P are positive, is discussed in §3. Case II, with real eigenvalues of E and negative Floquet multipliers of P , follows in §4. Case III, with complex eigenvalues of E and positive Floquet multipliers of P , forms the subject of §5. Results for the case where E has complex eigenvalues and P has negative Floquet multipliers follows without further work, since the location of E -homoclinics will be as in Case II and the location of P -homoclinic tangencies will be as in Case III.

We now summarise our main findings on the leading-order geometry and scaling laws of bifurcation sets; assumptions, derivation and details of these results are contained in §§3–7. We work in a two-parameter space, with parameters α and β . We

assume that an EP1t-cycle exists when $\alpha = 0$ and $\beta = 0$, and that α unfolds the codimension-one heteroclinic connection from E to P while β independently unfolds the heteroclinic tangency from P to E , as in Fig. 3.4. Thus, codimension-one connections from E to P occur on the β -axis, tangencies between $W^u(P)$ and $W^s(E)$ occur on the α -axis, and EP1-cycles occur on either the positive or negative β -axis. We use a constant k (if the eigenvalues of E are real) or \hat{k} (if E has a pair of complex eigenvalues) to indicate on which half of the β -axis the EP1-cycles occur; we define k or \hat{k} to be positive if transverse heteroclinic connections from P to E occur for $\beta < 0$.

We adopt the following notation: for E , λ and μ are the absolute values of the real parts of the leading stable and unstable eigenvalues, respectively; for P , the period of the orbit is $T = 2\pi/\Omega$ and the Floquet multipliers are $\tilde{L} = se^{-lT}$ and $\tilde{M} = se^{mT}$, where $s = \pm 1$ and l, m are real and positive. Moreover, $\delta_E \equiv \lambda/\mu$, $\delta_P \equiv l/m$ while \tilde{k} denotes either k or \hat{k} , depending on the case. The case of complex multipliers at P cannot occur in \mathbb{R}^3 if P is of saddle type.

All of the following results are for α and β small.

E -homoclinic orbits (Figs 3.5 and 4.2). E -homoclinic orbits occur at

$$\alpha = \alpha_n^\pm(\beta) = \alpha_n \left(1 \pm \frac{m}{\Omega} \sqrt{\frac{\beta_n - \beta}{\tilde{k}}} \right),$$

to lowest order, where $\alpha_n = KM^{-n}$, $\beta_n = SK^{\delta_P} \tilde{L}^n$, for constants K and S , and n is the (approximate) number of complete circuits that the E -homoclinic orbit makes in a neighbourhood of P .

Thus E -homoclinic orbits lie on a countable family of parabolas, with the different parabolas distinguished by the number of circuits n that the corresponding E -homoclinic orbits make about P . The family of parabolas accumulates on the half-line of EP1-cycles. To leading order as $n \rightarrow \infty$, the tips of the parabolas occur at $\alpha = KM^{-n}$, and lie on the curve $\beta = \text{sgn}(\alpha)S|\alpha|^{l/m}$. All the parabolas have the same orientation, with vertices pointing either up or down, depending on the sign of \tilde{k} . Different cases can be distinguished, depending on the Floquet multipliers at P . In \mathbb{R}^3 , since the flow around P must be orientation-preserving, and P is of saddle type, there are only two generic possibilities:

1. *Positive Floquet multipliers at P* : Here all parabola tips occur for the same sign of α . See Fig. 3.5.
2. *Negative Floquet multipliers at P* : The sign of α at which parabola tips occur alternates as n is incremented. See Fig. 4.2.

P -homoclinic tangencies (Figs 3.8, 5.2, 5.5 and 5.6). There are two cases, depending on the eigenvalues at the equilibrium.

1. *Real eigenvalues at E* : P -homoclinic tangencies occur for

$$\alpha = -\tilde{c}\beta^{\delta_E}, \quad \beta > 0,$$

to lowest order, where \tilde{c} is a constant; P -homoclinic orbits exist in the region bounded by this curve and the half lines $\alpha = 0$, $\beta < 0$ (if $k > 0$) or $\alpha = 0$, $\beta > 0$ (if $k < 0$) where EP1-cycles exist, and so are present on both sides of the α -axis only if $k > 0$. See Fig. 3.8.

2. *Complex eigenvalues at E* : P -homoclinic tangencies come (asymptotically) in two types, which we refer to as *tip*- and *side*-tangencies. Tip-tangencies lie

on a ‘snaking’ curve

$$\alpha = -\hat{c}\beta^{\delta_E} \cos\left(\hat{\Phi} - \frac{\omega}{\mu} \ln \beta\right), \quad \beta > 0,$$

where \hat{c} and $\hat{\Phi}$ are constants. At the folds of this curve the asymptotics are not valid. Side-tangencies occur on near-vertical curves, a pair of which emanates from the vicinity of each of the folds of the tip-tangency curves, oriented in the positive β -direction for $\hat{k} < 0$ and in the negative direction for $\hat{k} > 0$. P -homoclinic orbits exist at all points in the region bounded by the curves of tangencies, with many P -homoclinics coexisting in some regions. We refer to §5 for details. The overall picture is like the laying down of a long folded cloth, viewed from an oblique angle, with the fold length becoming zero as we approach the floor. See Figs 5.2, 5.5 and 5.6.

Fold bifurcations (Figs 6.3 and 6.4). We consider only positive Floquet multipliers at P . It is well-known that there must be infinitely many fold bifurcations (and also period-doubling bifurcations) at parameter values near a P -homoclinic tangency. On the other hand, in the case of complex eigenvalues at E with $\delta_E < 1$, there are infinitely many folds (and period-doublings) that accumulate on each E -homoclinic orbit. These two families of folds must somehow glue together at an EP1t-point. How this gluing occurs gives insight into a complete unfolding of the dynamics near the codimension-two point. There are several cases depending on the eigenvalues at E . The results for complex eigenvalues come from a simplification that we cannot rigorously justify in general, but nevertheless match the numerical results well in all cases.

1. *Real eigenvalues at E with $\delta_E < 1$.* Here each parabolic curve of E -homoclinic orbits has an *inclination flip* bifurcation near its tip where the twistedness of the global stable manifold of E around the E -homoclinic orbit changes. Such codimension-two bifurcations are each the root point of a curve of folds that is associated with the P -homoclinic tangency. See Fig. 6.3(a),(b).
2. *Real eigenvalues at E with $\delta_E > 1$.* This case is similar in that there is one curve of folds associated with each E -homoclinic parabola, but this fold remains close to one branch of the parabola rather than terminating at an inclination flip point. See Fig. 6.3(c),(d).
3. *Complex eigenvalues at E with $\delta_E > 1$.* This case is similar to case 2, although there *may* now be finitely many additional curves of folds associated with each E -homoclinic parabola, which disappear in pairs at cusp points. See Fig. 6.4(a).
4. *Complex eigenvalues at E with $\delta_E < 1$.* Here there are *infinitely* many curves of folds associated with each E -homoclinic parabola. The folds disappear in pairs at cusp points. See Fig. 6.4(b)–(d).

Homoclinic snaking (Figs 7.1–7.5). We give a geometric explanation of the homoclinic snaking phenomenon that has been observed in a number of examples. Our explanation is based on certain hypotheses about the properties of the heteroclinic connection from P to E . Specifically, we assume that as the parameter β varies there is a first and a last tangency between $W^u(P)$ and $W^s(E)$. The role of α is as before. Assuming a connection from E to P exists, transverse intersections between $W^u(P)$ and $W^s(E)$ will give rise to EP1-cycles and occur in pairs on an interval of the β -axis, while tangencies between $W^u(P)$ and $W^s(E)$ will correspond to EP1t-cycles and

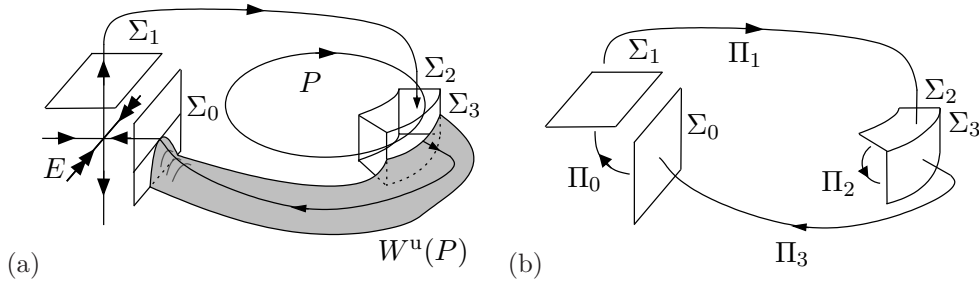


FIG. 3.1. Case I: (a) Sketch of phase space and sections at E and P ; the situation for $k < 0$ is shown. (b) Decomposition into local and global maps.

will occur at isolated points on the β -axis, including the endpoints of the interval of EP1-cycles. From this geometry we have two cases:

1. *Positive Floquet multipliers at P* : There is a single smooth curve of E -homoclinic orbits having one sign of α that accumulates on the curve of EP1-cycles. The curve of E -homoclinics has infinitely many extrema with respect to β , which converge on the EP1t-points in the manner described above in the local analysis. See Figs 7.3 and 7.4. Such a curve has been called a *homoclinic snake*.
2. *Negative Floquet multipliers at P* : There is one curve of E -homoclinic orbits in the (α, β) -plane for each sign of α . Each curve has infinitely many extrema with respect to β accumulating on each EP1t-point. See Fig. 7.5.

3. Case I: Real eigenvalues at E , positive Floquet multipliers at P . The assumptions we make in this case are as follows. The heteroclinic connections lie in the leading stable and unstable directions at E and P , where applicable, and the tangency of the stable manifold of E with the unstable manifold of P is quadratic. The Jacobian matrix of the flow evaluated at E has real distinct eigenvalues $\mu, -\lambda_1$ and $-\lambda_2$ satisfying $-\lambda_2 < -\lambda_1 < 0 < \mu$ and the non-resonance conditions

$$m_1\lambda_1 + m_2\lambda_2 - m_3\mu \notin \{-\mu, \lambda_1, \lambda_2\},$$

for all $m_1, m_2, m_3 \in \mathbb{N}$ satisfying $m_1 + m_2 + m_3 > 1$.

For the Floquet multipliers $\exp(-lT)$ and $\exp(mT)$ at P , where T is the period of P , the distinct rates l and m are (real) positive constants satisfying

$$m_1m - m_2l \notin \{m, -l\}$$

for all $m_1, m_2 \in \mathbb{N}$ with $m_1 + m_2 > 1$.

Finally, the underlying vector field is C^N smooth with N large enough for the results in [36] to apply near E and P with a C^1 conjugacy. See (3.1) and (3.3).

3.1. Map construction. We first construct local maps near E and P . Following Sternberg [36], the non-resonance assumption allows us to choose local coordinates (x, y, z) near E with the coordinate axes pointing in the directions of the associated eigenvectors so that the flow near E can be written as

$$\dot{x} = -\lambda_1 x, \quad \dot{y} = -\lambda_2 y, \quad \dot{z} = \mu z. \quad (3.1)$$

Cross-sections near E are defined using the local coordinates, i.e.,

$$\Sigma_0 = \{(x, y, z) \mid x = h_0\} \quad \text{and} \quad \Sigma_1 = \{(x, y, z) \mid z = h_1\},$$

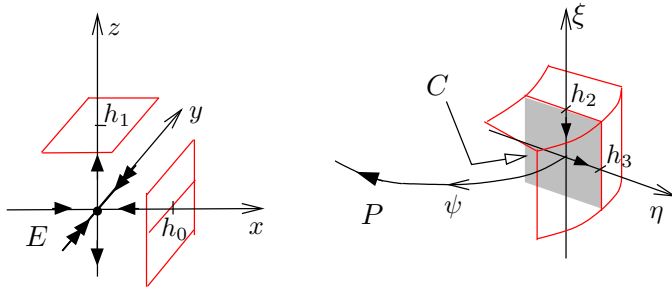


FIG. 3.2. Schematic diagram showing the local coordinate systems used near E and P .

where h_0 and h_1 are small positive constants. See Fig. 3.2. For sufficiently small h_0 and h_1 the flow induces a map from Σ_0 to Σ_1 . An approximation to the map is obtained by integrating equations (3.1). We obtain

$$\Pi_0(h_0, y, z) = \left(h_0 \left(\frac{z}{h_1} \right)^{\delta_E}, y \left(\frac{z}{h_1} \right)^{\hat{\delta}_E}, h_1 \right), \quad z > 0, \quad (3.2)$$

where

$$\delta_E = \lambda_1/\mu$$

measures the relative importance of the leading stable eigenvalue of E compared to its unstable eigenvalue, and

$$\hat{\delta}_E = \lambda_2/\mu > \delta_E.$$

We construct a local map near P in a similar way. To define local coordinates near P by smooth conjugacy, we note first that P can be parametrised by an angle ψ with $-\pi < \psi \leq \pi$ (we pick an origin for the ψ -coordinate below). Next, we define a cross-section C transverse to P at $\psi = 0$. Then $W^u(P)$ and $W^s(P)$ will intersect C on one-dimensional curves. We choose local coordinates (η, ξ) in C so that $W^u(P) \cap C$ and $W^s(P) \cap C$ are tangent to the coordinate axes, with the origin of each coordinate at $P \cap C$. See Fig. 3.2. We can extend these local coordinates to a neighbourhood of the whole of P by evolution under the flow in an obvious way. Our aim is to find coordinates in which the flow near P takes the form

$$\dot{\psi} = \Omega, \quad \dot{\eta} = m\eta, \quad \dot{\xi} = -l\xi, \quad (3.3)$$

where $\Omega \equiv 2\pi/T$ with T the period of P .

To do so, we choose coordinates that trivialise the ψ dynamics by straightening stable and unstable fibers (see, e.g., Lemma 1 in [2] for a symmetric version of this procedure) and by rescaling time with a suitable Euler multiplier. In the resulting planar system we choose coordinates that linearise the hyperbolic period- T map; the non-resonance assumption on l and m guarantees that this is possible. See, e.g., [36]. Finally, we note that this period- T map is trivially generated by (3.3) and we can pull back the coordinate change to the full space.

We define further cross-sections near P using the local coordinates:

$$\Sigma_2 = \{(\psi, \eta, \xi) \mid \xi = h_2\} \quad \text{and} \quad \Sigma_3 = \{(\psi, \eta, \xi) \mid \eta = h_3\},$$

where h_2 and h_3 are small positive constants (we will constrain the constant h_2 further, as discussed below). For sufficiently small h_2 and h_3 , the flow near P induces a map from Σ_2 to Σ_3 , with an approximation to the map being obtained by integrating equations (3.3). To lowest order, we find

$$\Pi_2(\psi, \eta, h_2) = \left(\left[\psi - \frac{\Omega}{m} \ln \left(\frac{\eta}{h_3} \right) \right] \bmod 2\pi, h_3, h_2 \left(\frac{\eta}{h_3} \right)^{\delta_P} \right), \quad \eta > 0, \quad (3.4)$$

where

$$\delta_P = l/m$$

measures the relative importance of the stable Floquet exponent compared with the unstable exponent.

We next construct the global maps. First, we define a map $\Pi_1 : \Sigma_1 \rightarrow \Sigma_2$ that approximates the dynamics near the heteroclinic connection from E to P . The connection, when it occurs, is one-dimensional, intersecting Σ_1 at $(x, y, z) = (0, 0, h_1)$ and intersecting Σ_2 at $(\psi, \eta, \xi) = (\bar{\psi}, 0, h_2)$, where $\bar{\psi}$ is a real constant. The connection is of codimension one, and we introduce a real parameter α that unfolds the heteroclinic bifurcation, which we assume to occur at $\alpha = 0$. Retaining just the lowest order terms in x , y and α , in the standard way, we obtain the map

$$\Pi_1(x, y, h_1) = (\bar{\psi} + ax + by + f\alpha, cx + dy + \alpha, h_2), \quad (3.5)$$

where a, b, c, d, f are generically non-zero constants with $ad - bc \neq 0$, and where we have chosen a scaling so that α has a coefficient 1 in the expression $cx + dy + \alpha$. As we will see later, we are free to set $\bar{\psi} = 0$.

We now derive a map $\Pi_3 : \Sigma_3 \rightarrow \Sigma_0$ that approximates the dynamics near a heteroclinic tangency between $W^u(P)$ and $W^s(E)$. The tangency generically will be of codimension one and so we introduce a real parameter β to unfold the heteroclinic tangency, which we assume to occur at $\beta = 0$, as illustrated in Fig. 3.3.

So far we have not specified an origin for the ψ -coordinate near P . We now pick the origin of ψ in Σ_3 to correspond to the heteroclinic tangency between $W^u(P)$ and $W^s(E)$. Then, when $\beta = 0$, the heteroclinic tangency intersects Σ_3 at $(\psi, \eta, \xi) = (0, h_3, 0)$ and intersects Σ_0 at $(x, y, z) = (h_0, \bar{y}, 0)$ for some constant \bar{y} . Since ψ parametrises $W^u(P) \cap \Sigma_3$ and since the tangency between $W^u(P)$ and $W^s(E)$ is generically quadratic, the y - and z -coordinates of $W^u(P) \cap \Sigma_0$ near the tangency can be written as

$$y = \bar{y} + g\psi, \quad z = k\psi^2,$$

to lowest order in ψ , where g and k are constants with $k \neq 0$. Note that ψ is small near the tangency, although not small over a full neighbourhood of P . In the standard way, we extend to orbits near the heteroclinic tangency and express the map Π_3 to lowest order in ψ , ξ and β as follows:

$$\Pi_3(\psi, h_3, \xi) = (h_0, \bar{y} + g\psi + q\xi + r\beta, k\psi^2 + s\xi + \beta + v\beta\psi), \quad (3.6)$$

where q, r, s, v are constants with $q - rs \neq 0$, and where we have chosen a scaling so that β has coefficient 1 in the expression $k\psi^2 + s\xi + \beta + v\beta\psi$.

Having fixed the origin of the ψ coordinate near P , we now pick h_2 , the constant determining the surface Σ_2 , to simplify the geometry and maps further. Specifically,

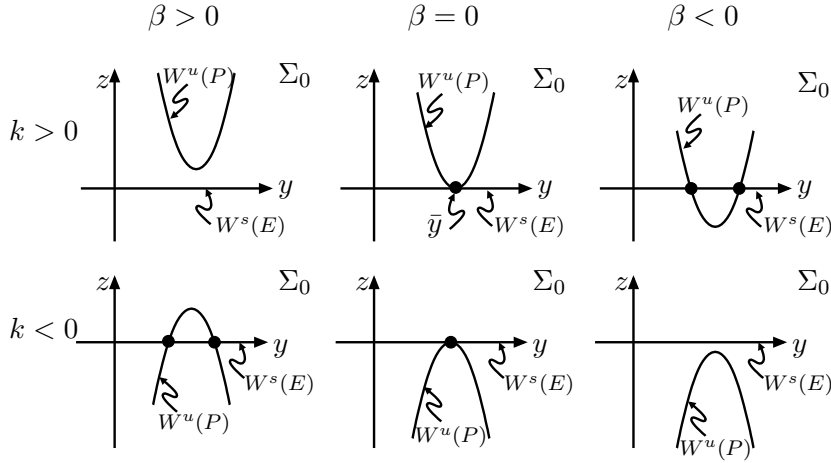


FIG. 3.3. Case I: Unfolding a heteroclinic tangency between $W^u(P)$ and $W^s(E)$. Each panel shows the relative positions of $W^u(P) \cap \Sigma_0$ and $W^s(E) \cap \Sigma_0$. The upper row has $k > 0$, lower row $k < 0$. Left column has $\beta > 0$, middle $\beta = 0$, right $\beta < 0$. The large dots correspond to heteroclinic orbits from P to E .

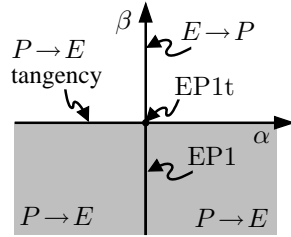


FIG. 3.4. Locations of heteroclinic connections, cycles and tangencies in the (α, β) -plane for $k > 0$ in the case that E has real eigenvalues. When E has complex eigenvalues, this sketch corresponds to the case $\hat{k} > 0$, as discussed in §5.

we pick h_2 so that $\bar{\psi} = 0$, i.e., so that when the heteroclinic connection from E to P occurs, the phase of the heteroclinic connection is zero at the point where it crosses Σ_2 . This ensures that the cross-sections Σ_2 and Σ_3 are centred about the same ψ value, which greatly simplifies the analysis near P , particularly in the case of negative Floquet multipliers of P , as discussed in §4. We note that it is possible to satisfy this constraint on h_2 while picking h_2 arbitrarily small.

Figure 3.4 summarises the consequences of the assumptions built into our map construction for the location in the (α, β) -plane of the various heteroclinic connections and cycles. Consider the case $k > 0$ (the case $k < 0$ is obtained simply by reflection about the α -axis). The codimension-two EP1t-cycle occurs at the origin. For every point in the negative β half-plane, there exists at least one heteroclinic connection from P to E . These are robust as codimension-zero objects, and become heteroclinic tangencies when β is zero. The codimension-one heteroclinic connections from E to P occur on the β -axis and so EP1-cycles occur on the negative β -axis.

3.2. E -homoclinic bifurcations. We use the maps derived above to locate E -homoclinics near the EP1t-point. In terms of local coordinates near E , an E -

homoclinic first crosses Σ_1 at $(0, 0, h_1)$ and returns to Σ_0 with z -coordinate equal to zero. Thus we find E -homoclinics by equating to zero the z -component of $\Pi_3 \circ \Pi_2 \circ \Pi_1(0, 0, h_1)$. We find that the following approximate equation must be satisfied if an E -homoclinic is to exist:

$$k \left[\left(\Psi + f\alpha - \frac{\Omega}{m} \ln \alpha \right) \bmod 2\pi \right]^2 - S\alpha^{\delta_P} + \beta + v\beta \left[\left(\Psi + f\alpha - \frac{\Omega}{m} \ln \alpha \right) \bmod 2\pi \right] = 0, \quad (3.7)$$

where $S = -sh_2h_3^{-\delta_P}$, and $\Psi = (\Omega/m) \ln h_3$. Solutions of this equation are given by

$$\left(\Psi + f\alpha - \frac{\Omega}{m} \ln \alpha \right) \bmod 2\pi = -\frac{v\beta}{2k} \pm \frac{1}{2} \sqrt{\frac{v^2\beta^2}{k^2} + \frac{4}{k}(S\alpha^{\delta_P} - \beta)}. \quad (3.8)$$

We expand (3.8) to obtain, to lowest order,

$$\Psi - \frac{\Omega}{m} \ln \alpha = 2n\pi - \frac{v\beta}{2k} \pm \sqrt{\frac{S}{k}\alpha^{\delta_P} - \frac{\beta}{k}}, \quad (3.9)$$

where n is an integer counting the number of times the homoclinic orbit winds around P . There are double roots on the right-hand side of (3.9) when $\beta = S\alpha^{\delta_P}$. Thus, when $k > 0$, E -homoclinics exist only for $\beta < S\alpha^{\delta_P}$, to leading order, and annihilate pairwise on the curve $\beta = S\alpha^{\delta_P}$, $\alpha > 0$. Rearranging equation (3.9) we find that the annihilation points occur, to leading order, at

$$\alpha = \alpha_n = KM^{-n}, \quad \beta = \beta_n = SK^{\delta_P}L^n,$$

where $K = \exp(\Psi m/\Omega)$, $M = \exp(2m\pi/\Omega)$ and $L = \exp(-2l\pi/\Omega)$. In these expressions M and L are, respectively, the unstable and stable Floquet multipliers of P . At $\alpha = \alpha_n$, two solutions emerge for varying β for approximately the same value of α . Specifically, substituting $\beta \approx \beta_n$ and expanding, we find curves

$$\alpha_n^\pm(\beta) = \alpha_n \left(1 \pm \frac{m}{\Omega} \sqrt{\frac{\beta_n - \beta}{k}} \right)$$

so that the sign of $\beta - \beta_n$ is opposite to that of k . In fact there are eight distinct cases depending on the signs of $\delta_P - 1$, S and k . See Fig. 3.5.

These conclusions are in accord with the results on non-wandering sets in [25]: the region in which E -homoclinic orbits exist, bounded by the envelope curve and the β -axis, lies in the complement of the region for which [25] finds the non-wandering set to be trivial (compare Fig. 3.8 for $S > 0, k > 0$ with Fig. 2 in [25]).

3.3. P -homoclinic bifurcations. In terms of local coordinates near P , a P -homoclinic orbit first crosses Σ_3 with $\xi = 0$ and returns to Σ_2 with $\eta = 0$. Thus, P -homoclinics are found by equating to zero the η -component of $\Pi_1 \circ \Pi_0 \circ \Pi_3(\psi, h_3, 0)$:

$$\eta = \alpha + \tilde{c}Z^{\delta_E} + \tilde{d}(\bar{y} + g\psi + r\beta)Z^{\hat{\delta}_E} = 0, \quad (3.10)$$

where $Z := k\psi^2 + \beta + v\beta\psi$, $\tilde{c} = ch_0h_1^{-\delta_E}$, $\tilde{d} = dh_1^{-\hat{\delta}_E}$. Equation (3.10) yields a function $\alpha = \alpha(\beta, \psi)$, valid only for $Z > 0$. Since $\hat{\delta}_E > \delta_E$, equation (3.10) implies that

$$\alpha(\beta, \psi) = -\tilde{c}Z^{\delta_E} + O\left(Z^{\hat{\delta}_E}\right), \quad (3.11)$$

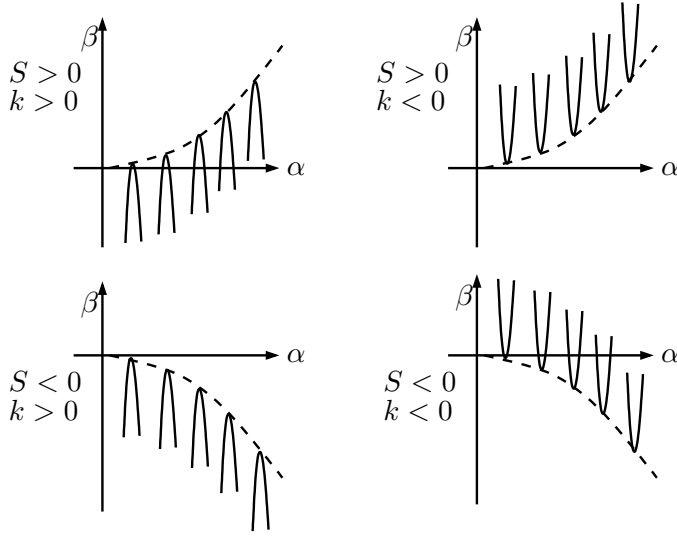


FIG. 3.5. Case I: E -homoclinic orbits occur locally on the solid curves. All panels show the case $\delta_P > 1$; the case $\delta_P < 1$ differs only in the shape of the dashed curve $\beta = S\alpha^{\delta_P}$, which is the envelope of the folds of E -homoclinic loci.

and hence that the sign of α for which P -homoclinics exist is that of $-c$. Homoclinic tangencies between $W^u(P)$ and $W^s(P)$, for which the manifolds are in the configuration shown in the middle column of Fig. 3.6, must satisfy $\partial\alpha/\partial\psi = 0$, i.e.,

$$-\tilde{c}\delta_E Z^{\delta_E-1} Z' = 0, \quad (3.12)$$

where $Z' \equiv dZ/d\psi = 2k\psi + v\beta$. Thus for $Z > 0$ homoclinic tangencies occur at $\psi = \bar{\psi} \equiv -v\beta/2k$. At this point $Z = \beta$ to leading order, and it follows from (3.11) that such tangencies occur, to leading order, along the curve

$$\alpha = -\tilde{c}\beta^{\delta_E}, \quad \beta > 0, \quad (3.13)$$

in the (α, β) -plane emanating from the EP1t-point. On this curve, the sheet of P -homoclinics parametrised by α and β has a smooth fold.

To determine the location of the nearby P -homoclinics we fix a value of α and define $\beta = \bar{\beta}(\alpha)$ to be the value of β at which the homoclinic tangency occurs. Using a Taylor expansion, equation (3.10) can now be rewritten, for $|\beta - \bar{\beta}| \ll 1$, $|\psi - \bar{\psi}| \ll 1$ as well as $\beta \ll 1$, in the form

$$\eta = \delta_E \tilde{c} \bar{\beta}^{\delta_E-1} [k(\psi - \bar{\psi})^2 + \beta - \bar{\beta}], \quad (3.14)$$

again to leading order. It follows that $W^u(P) \cap \Sigma_2$ is oriented in the manner shown in Fig. 3.6. For example, for $c > 0$, $k > 0$ and $\beta < \bar{\beta}$, $W^u(P)$ has a local minimum that falls below $\eta = 0$ and a pair of homoclinics is present. These are destroyed at the tangency as β increases through $\bar{\beta}$. For $c < 0$, $k > 0$ and $\beta < \bar{\beta}$, $W^u(P)$ has a local maximum which lies above $\eta = 0$ and a pair of homoclinics is again present; these are destroyed at the tangency as β increases. The corresponding results for other combinations of the signs of c and k can be easily computed.

It is clear from equation (3.10) that, if $c \neq 0$, P -homoclinics can exist for $\alpha < 0$ or $\alpha > 0$ (if $c > 0$ or $c < 0$, respectively) but not both. Assuming $c > 0$, $k > 0$ and

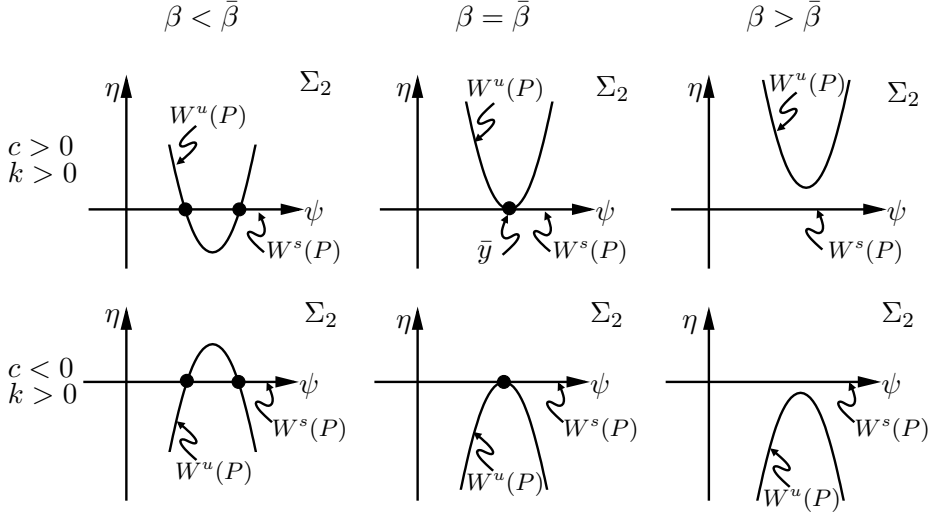


FIG. 3.6. Case I: Unfolding a homoclinic tangency between $W^u(P)$ and $W^s(P)$ for fixed, non-zero α . Each panel shows the relative positions of $W^u(P) \cap \Sigma_2$ and $W^s(P) \cap \Sigma_2$. At tangency, $\beta = \bar{\beta}(\alpha) \equiv (-\alpha/\tilde{c})^{1/\delta_E}$, to lowest order. The upper row has $c > 0, k > 0$, while the lower row has $c < 0, k > 0$. The left column is for $\beta < \bar{\beta}$, the middle column for $\beta = \bar{\beta}$, and the right one for $\beta > \bar{\beta}$. The large dots correspond to orbits homoclinic to P . The cases $c > 0, k < 0$ ($c > 0, k < 0$) locally look like the lower (upper) row but with the left and right columns interchanged. For $k < 0$, see also Fig. 3.7.

examining (3.11) in the limit $\alpha \rightarrow 0$ from below and $\beta > 0$ fixed, we see that $Z \rightarrow 0$ from above, i.e., the P -homoclinic orbits approach the heteroclinic connection from P to E . At $\alpha = 0$, P -homoclinics cease to exist when they collide with $W^s(E)$ and so cannot escape from E to return to a neighbourhood of P . In parameter space, this occurs on the half of the β -axis where EP1 cycles occur ($\beta > 0$); along this half-line, two sheets of P -homoclinics meet in a cusp. Similar arguments apply to other combinations of the signs of c and k .

The case $k < 0$ can be analyzed further, because then $W^u(P) \cap \Sigma_2$ is a closed curve that shrinks to a point as $\beta \rightarrow 0$. The shape of $W^u(P)$ where it intersects various cross-sections is shown schematically in Fig. 3.7. Panel (b) depicts the non-degenerate linear image of $W^u(P)$ within Σ_1 , which is the union of two graphs $y(x)$, each of which is the union of one convex and one concave piece. P -homoclinics occur when the closed curve in panel (c) or (d) of this figure intersects the ψ -axis. The large dots in panels (c) and (d) mark the intersection of $W^u(E)$ with Σ_2 ; these points are approached along $W^u(P) \cap \Sigma_2$ as $Z \rightarrow 0$. Boxes mark extremal points in the η -direction, which produce folds of P -homoclinics as they cross the ψ -axis. Due to the convex-concave shape of $W^u(P) \cap \Sigma_2$ the number of such points cannot exceed three and depends on the orientation of $W^u(P) \cap \Sigma_2$ (which depends on Π_1) and its detailed shape (which depends on β). Depending on these details which we do not analyze here, the above leading-order result may be augmented by two additional curves of folds in the (α, β) -plane, with the curves possibly ending at a cusp point.

In summary, there are four possible (leading-order) bifurcation sets for P -homoclinic orbits, as shown in Fig. 3.8. With regard to the results on non-wandering sets in [25], the region of P -homoclinic orbits lies in the region for which the non-wandering set is non-trivial, and contains the region for which there exists a “basic set”. The

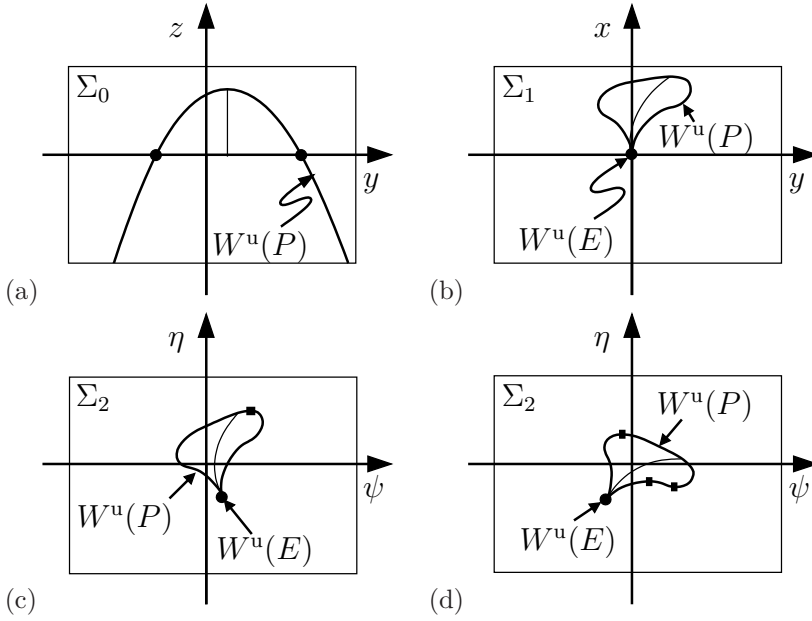


FIG. 3.7. Case I, $k < 0$: Sketch of the images on various cross-sections of $W^u(P)$ (bold curve) and of the line $\{y = \bar{y} + r\beta\} \subset \Sigma_0$ to which $W^u(P) \cap \Sigma_0$ degenerates for $g = 0$ (thin line). The large dots in panel (a) mark points where $Z = 0$, which are heteroclinic connections from P to E . In panels (b)-(d), the large dots show the intersection of $W^u(E)$ with the cross-section, which are approached as $Z \rightarrow 0$, and in (c) and (d) have $\eta = \alpha$. Panels (c) and (d) show different possible locations and orientations of $W^u(P)$ in Σ_2 . Here boxes denote extremal points in the η -direction which produce folds of P -homoclinics when they cross the ψ -axis.

latter is an invariant hyperbolic transitive set coinciding with the closure of its periodic orbits (compare Fig. 3.8 for $c < 0$, $k > 0$, $\delta_E < 1$ with Fig. 2 in [25]).

4. Case II: Real eigenvalues at E , negative Floquet multipliers at P .

The underlying assumptions for this case are as in Case I, except that the Floquet multipliers are $-\exp(-lT)$ and $-\exp(mT)$.

In \mathbb{R}^3 , either both Floquet multipliers of P are negative or neither of them is negative. In our construction of the map Π_3 in the case that both Floquet multipliers are positive, we assumed that, near tangency, orbits crossing Σ_3 with $\xi > 0$ last crossed Σ_2 with $\eta > 0$. This is not necessarily the case if both Floquet multipliers of P are negative, since some of the orbits crossing Σ_3 will have crossed Σ_2 with negative η , traversing P an odd number of times before crossing Σ_3 . We need to modify our construction of the local map Π_2 to allow for this possibility. The other maps are not affected by the sign of the Floquet multipliers.

A convenient global neighbourhood of P in the case of negative Floquet multipliers is a twisted tube whose normal cross-sections are rectangles, each with a centre point on P at some phase ψ . Such a tube would have only two surfaces, with ‘top’ and ‘bottom’ of each rectangle lying on the same surface, and ‘left’ and ‘right’ sides both lying on the other surface. However, since we are only interested in orbits close to the heteroclinic orbit with asymptotic phase zero at P , the neighbourhood of P and corresponding cross-sections need to be defined only locally, i.e., near $\psi = 0$.

To construct a modified local map near P , we have to keep track of changes in the

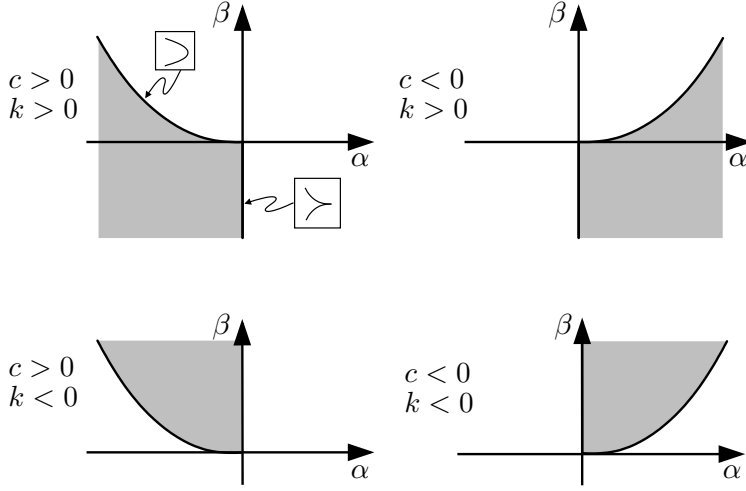


FIG. 3.8. Case I: Partial bifurcation set for P -homoclinic orbits for $\delta_E < 1$. Each panel shows the locus of homoclinic tangencies ($\alpha = -\tilde{c}\beta^{\delta_E}$, to leading order), where the sheet of P -homoclinic solutions folds smoothly (inset in upper left panel), and the part of the β -axis where this sheet ends at $EP1$ -cycles in a line of cusps (inset in upper left panel). The shading indicates to which side of the tangency or cusps the sheet extends, i.e., where the transverse homoclinic orbits exist.

sign of the η -component as mentioned above. Sign changes in η within the in-going cross-section give corresponding sign changes in ξ within the out-going cross-section. See Fig. 4.1. Therefore, we define the map $\hat{\Pi}_2 : \tilde{\Sigma}_2 \rightarrow \Sigma_3$, where $\tilde{\Sigma}_2$ is the preimage of Σ_3 in Σ_2 under the backward flow, by

$$\hat{\Pi}_2(\psi, \eta, h_2) = \left(\psi - \frac{\Omega}{m} \ln \left(\frac{|\eta|}{h_3} \right) - 2n\pi, h_3, \text{sgn}(\eta)h_2 \left(\frac{|\eta|}{h_3} \right)^{\delta_P} \right).$$

The map is not defined if $\eta = 0$. The quantity n is a positive integer and counts the number of complete circuits of P made by an orbit in passing from Σ_2 to Σ_3 ; it is even for $\eta > 0$ and odd for $\eta < 0$.

Similar calculations to those in §3.2 yield the loci of E -homoclinic bifurcations. These occur, at leading order, when

$$\Psi - \frac{\Omega}{m} \ln(|\alpha|) = 2\pi n - \frac{v\beta}{2k} \pm \sqrt{\frac{S}{k} \text{sgn}(\alpha) |\alpha|^{\delta_P} - \frac{\beta}{k}}.$$

Turning points in the E -homoclinic locus occur when the discriminant vanishes, i.e.,

$$\beta = \text{sgn}(\alpha) S |\alpha|^{\delta_P}.$$

Successive turning points occurring at (α_n, β_n) are naturally enumerated by integers $n \geq n_0$ for some large positive n_0 , in such a way that odd n is equivalent to negative α . In terms of the Floquet multipliers, we compute

$$\alpha_n = (-1)^n K M^{-n}, \quad \beta_n = (-1)^n S K^{\delta_P} L^n,$$

so the signs of α and β both switch as n is incremented. The direction of the folds is determined by the sign of the coefficient of β in the discriminant, i.e., by the sign of $-k$, as in §3.2. The corresponding bifurcation sets are sketched in Fig. 4.2.

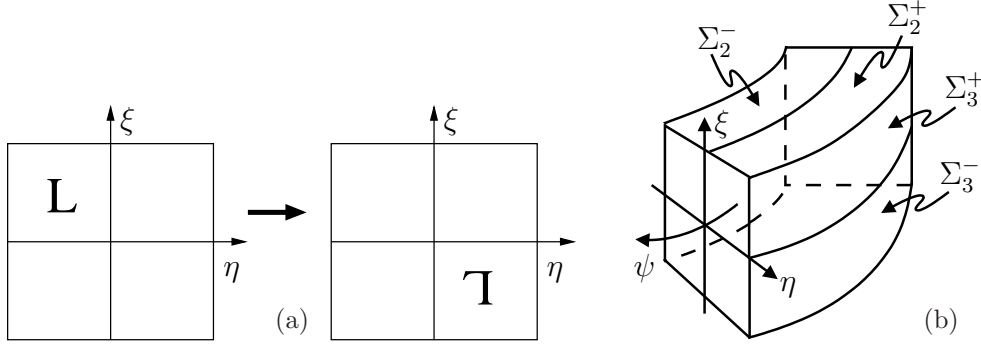


FIG. 4.1. Illustrating the dynamics in a neighbourhood of P in the case of negative Floquet multipliers. (a) The image of a section defined by $\{\psi = \text{const}\}$ under the flow once around P . (b) The relation of the signs of η in $\Sigma_2^+ \cup \Sigma_2^-$ and ξ in $\Sigma_3^+ \cup \Sigma_3^-$. Here $\eta < 0$ in Σ_2^- and $\xi < 0$ in Σ_3^- : $\hat{\Pi}_2$ maps Σ_2^- to Σ_3^- for an odd number of windings about P and maps Σ_2^+ to Σ_3^+ for an even number.

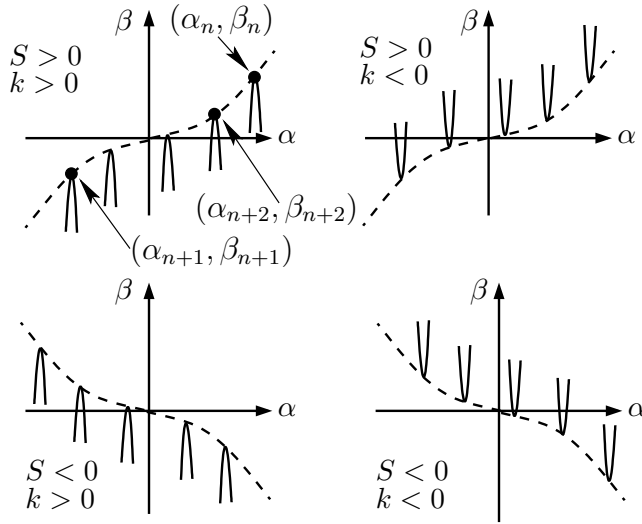


FIG. 4.2. Case II: E -homoclinic orbits occur locally on the solid curves. All panels show the case $\delta_P > 1$; the case $\delta_P < 1$ differs only in the shape of the dashed curve $\beta = \text{sgn}(\alpha)S|\alpha|^{\delta_P}$, which is the envelope of the folds of the E -homoclinic loci.

The locus of the homoclinic bifurcations of P will be unaffected by this modification of the map Π_2 (since Π_2 was not used in our calculations) and will remain as computed in §3.3, although the dynamics associated with the homoclinic bifurcations (e.g., the bifurcations of nearby periodic orbits) may change.

5. Case III: Complex eigenvalues at E , positive Floquet multipliers at P . The assumptions for this case are those of Case I except that the Jacobian matrix of the flow evaluated at E has eigenvalues μ , $-\lambda \pm i\omega$ with distinct $\mu > 0$, $\lambda > 0$, and ω a positive constant.

The local map Π_0 needs to be modified to cover the case where the Jacobian matrix of the flow evaluated at E has complex eigenvalues. This modification will

affect the locus of P -homoclinic tangencies, but not of E -homoclinic bifurcations (which will remain as calculated in §3.2). The behaviour of periodic orbits associated with the homoclinic bifurcations of both E and P may be affected. The calculation that follows is an adaptation of that in [16] for the Shil'nikov-Hopf bifurcation.

To obtain the modified version of Π_0 we use local polar coordinates (r, θ, z) near E chosen so that the flow near E can be written as

$$\dot{r} = -\lambda r, \quad \dot{\theta} = \omega, \quad \dot{z} = \mu z. \quad (5.1)$$

The non-resonance assumptions on λ and μ guarantee that this is possible. Since we are using polar coordinates it is convenient to define a new cross-section

$$\hat{\Sigma}_0 = \{(r, \theta, z) \mid r = h_0\},$$

for h_0 a small positive constant. The cross-section Σ_1 defined earlier does not require modification. For sufficiently small h_0 and h_1 the flow then induces a map from $\hat{\Sigma}_0$ to Σ_1 . Using (5.1) we find to lowest order:

$$\begin{aligned} \hat{\Pi}_0(h_0, \theta, z) = & \left(\tilde{h} z^{\delta_E} \cos \left(\theta - \frac{\omega}{\mu} \ln \left(\frac{z}{h_1} \right) \right), \right. \\ & \left. \tilde{h} z^{\delta_E} \sin \left(\theta - \frac{\omega}{\mu} \ln \left(\frac{z}{h_1} \right) \right), h_1 \right), \quad z > 0, \end{aligned}$$

where $\tilde{h} = h_0 h_1^{-\delta_E}$, and

$$\delta_E = \frac{\lambda}{\mu}$$

plays a role equivalent to that in the real eigenvalue case.

The cross-section $\hat{\Sigma}_0$ is also used in the derivation of the global map Π_3 . Arguing as in our derivation of Π_3 we compute the modified global map $\hat{\Pi}_3 : \Sigma_3 \rightarrow \hat{\Sigma}_0$, which approximates the dynamics near a heteroclinic tangency between $W^u(P)$ and $W^s(E)$. To lowest order in ψ , ξ and β , we find

$$\hat{\Pi}_3 : (\psi, h_3, \xi) \mapsto (h_0, \theta, z) \quad (5.2)$$

$$= (h_0, \hat{g}\psi + \hat{q}\xi + \hat{r}\beta, \hat{k}\psi^2 + \hat{s}\xi + \beta + \hat{v}\beta\psi), \quad (5.3)$$

where $\hat{g}, \hat{q}, \hat{r}, \hat{k}, \hat{s}, \hat{v}$ are constants with $\hat{k} \neq 0$. In calculating this map we have chosen the origin of the θ coordinate near E so that the heteroclinic tangency intersects $\hat{\Sigma}_0$ with $\theta = 0$.

To locate P -homoclinics we first appeal to the geometry of $W^u(P) \cap \Sigma_2$ shown in Figs 5.1, 5.3, 5.4 and schematically in Fig. 5.2. The image of $W^u(P)$ in Σ_0 is a parabola by assumption, whose extremum occurs when the ψ -coordinate (in Σ_3 ; ψ parametrises $W^u(P) \cap \Sigma_3$) takes the value $\psi = -v\beta/2\hat{k}$. The z -coordinate of the extremum is $O(\beta)$. The image in Σ_1 of this parabola bounds a spiral-shaped region with round tip. An affine map takes the spiral from Σ_1 to Σ_2 , preserving its topological properties, so that the parameter β winds or unwinds the spiral region and controls its thickness, while α moves the core of the spiral in the (η, ψ) -plane (in Σ_2) in the direction $(1, f)$. The parameter \hat{k} determines the direction of folding at the spiral tip. Thus, for $\hat{k} > 0, \beta > 0$, the tip is the inner end of the spiral, and the spiral has finitely many windings (see Fig. 5.3) while for $\hat{k} < 0, \beta > 0$ the tip is the outer end of the

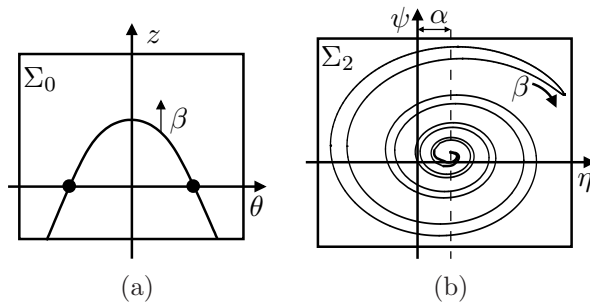


FIG. 5.1. Case III with $\hat{k} < 0, \beta > 0$: Sketches of (a) $W^u(P) \cap \Sigma_0$, and (b) $W^u(P) \cap \Sigma_2$. The case in (b) is near a side-tangency; spiralling continues into the point $(\alpha, f\alpha)$, which is the image of $W^u(E)$. The indicated direction of tip motion/rotation is for increasing β .

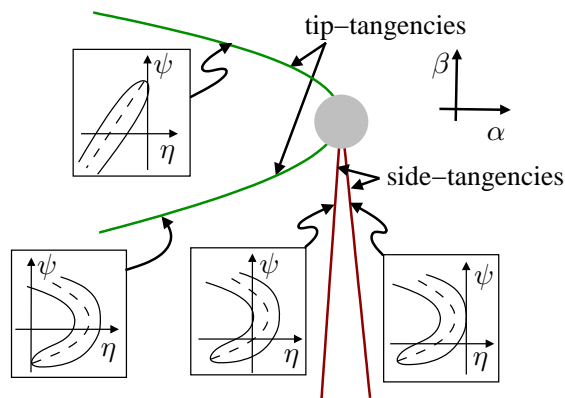


FIG. 5.2. Case III with $\beta > 0$ and $\hat{k} < 0$ (for $\hat{k} > 0$ reflect about the α -axis): A sketch of the types of homoclinic tangencies in the (α, β) -plane in a region of parameter space in which curves of tip- and side-tangencies approach one another. Bold curves form the local parameter set of tangencies: tip-tangencies (green) and side-tangencies (red). Insets show the relevant part of $W^u(P) \cap \Sigma_2$, with the dashed line being the center of the parabola onto which $W^u(P) \cap \Sigma_2$ collapses for $\hat{g} = 0$. The grey shading indicates the region in which it is not useful to distinguish between the two types of tangency.

spiral, the spiral has infinitely many windings and is centred on the point $(\alpha, f\alpha)$ (see Fig. 5.1). For $\hat{k} > 0, \beta < 0$ the spiral again has infinitely many windings but the tip is now at $(\alpha, f\alpha)$ at the core of the spiral (see Fig. 5.4). In the case $\hat{k} < 0, \beta < 0$ there are (locally) no intersections between $W^u(P)$ and Σ_2 .

Intersections of $W^u(P) \cap \Sigma_2$ with $\eta = 0$ correspond to P -homoclinic orbits, which are created or destroyed as either the spiral tip or one of its sides crosses the line $\eta = 0$. We distinguish between *tip-tangency*, primarily controlled by varying β , and *side-tangency* primarily controlled by varying α (see Figs 5.2 and 5.3). The geometry of these tangencies is shown in Fig. 5.2. The distinction between tip- and side-tangencies becomes invalid near places where the two types of tangency coincide, as will be discussed further below.

We investigate further the nature of P -homoclinic tangencies by analysing the maps derived above. To locate the tangencies we compute $\Pi_1 \circ \hat{\Pi}_0 \circ \hat{\Pi}_3(\psi, h_3, 0)$ and equate to zero the η -component of this expression and also its derivative with respect

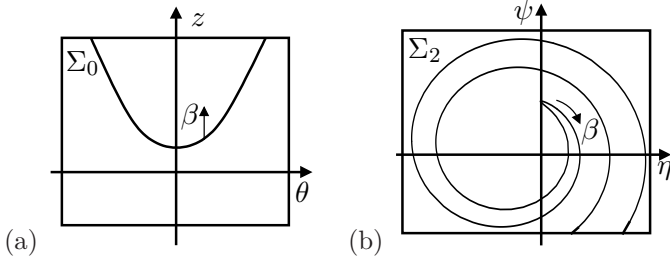


FIG. 5.3. Case III with $\hat{k} > 0$, $\beta > 0$: Sketches of (a) $W^u(P) \cap \Sigma_0$, (b) $W^u(P) \cap \Sigma_2$ near P at a tip-tangency. The indicated direction of tip motion/rotation is for increasing β .

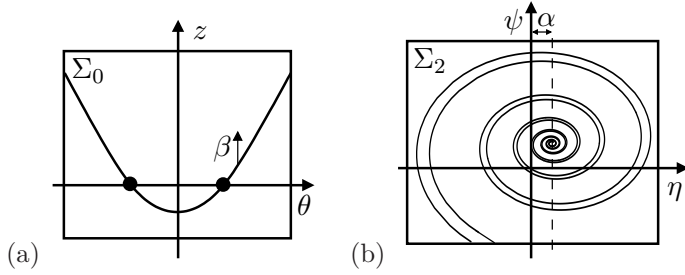


FIG. 5.4. Case III with $\hat{k} > 0$, $\beta < 0$: Sketches of (a) $W^u(P) \cap \Sigma_0$, (b) $W^u(P) \cap \Sigma_2$ near P . Spiralling continues into the point $(\alpha, f\alpha)$ which is the image of $W^u(E)$ and the bullets plotted in (a).

to ψ . We find that intersections between $W^u(P)$ and $W^s(P)$ occur, to lowest order, for

$$\alpha = \alpha(\psi, \beta) = -\hat{c}Z^{\delta_E} \cos A, \quad (5.4)$$

where

$$Z := \hat{k}\psi^2 + \beta + \hat{v}\beta\psi, \quad A := \hat{\Phi} + \hat{g}\psi + \hat{r}\beta - \frac{\omega}{\mu} \ln Z$$

and $\hat{c} = h_0 h_1^{-\lambda/\mu} \sqrt{c^2 + d^2} > 0$, $\hat{\Phi} = \tan^{-1}(-d/c) + (\omega/\mu) \ln h_1$. Expression (5.4) is valid only if $Z > 0$. To find the P -homoclinic tangencies, we need to solve $d\alpha/d\psi = 0$ for α satisfying (5.4), which reduces to solving

$$\delta_E Z' \cos A - \left(\hat{g}Z - \frac{\omega}{\mu} Z' \right) \sin A = 0 \quad (5.5)$$

for ψ , where $Z' \equiv dZ/d\psi$. We can understand the nature of the solutions to this equation by first examining the special case $\hat{g} = 0$, and then incorporating small values of \hat{g} . When $\hat{g} = 0$, equation (5.5) reduces to

$$\frac{1}{\mu} Z' (\lambda \cos A + \omega \sin A) = 0. \quad (5.6)$$

The solutions with $Z' = 0$ correspond to tip tangencies while those with $\tan A = -\lambda/\omega$, $Z' \neq 0$, correspond to side tangencies. We examine these two possibilities in turn.

For the tip tangencies, $Z' = 0$, we obtain $\psi = -\hat{v}\beta/2\hat{k}$ and hence $Z = \beta + O(\beta^2)$, $A = \hat{\Phi} - \frac{\omega}{\mu} \ln \beta + O(\beta)$. From equation (5.4) it now follows that tip tangencies occur when

$$\alpha = -\hat{c}\beta^{\delta_E} \cos\left(\hat{\Phi} - \frac{\omega}{\mu} \ln \beta\right) + O(\beta^{1+\delta_E}), \quad (5.7)$$

where the coefficient of the $O(\beta^{1+\delta_E})$ term vanishes at $\hat{v} = \hat{r} = 0$. Thus the case $0 < \hat{g} \ll 1$ corresponds to a small perturbation of the snaking curve arising in Shil'nikov dynamics [13]. At this order, the sign of $\hat{k} > 0$ does not affect the position of tip tangencies, although it does determine which side of these tangencies (in the (α, β) -plane) homoclinic solutions exist.

In contrast, for the side tangencies we obtain

$$\hat{\Phi} + \hat{r}\beta - \frac{\omega}{\mu} \ln Z = -\arctan\left(\frac{\lambda}{\omega}\right) + n\pi, \quad (5.8)$$

where by \arctan we mean the principal value in $(-\pi/2, \pi/2]$, and $n > 0$ measures the number of multiples of π required to reach equality in this expression, i.e., n measures the number of oscillations the tangent P -homoclinic orbit makes close to E . Hence

$$Z = Z_n \equiv A_n e^{\hat{r}\beta\mu/\omega}, \quad (5.9)$$

where $A_n := e^{(\bar{\Phi}-n\pi)\mu/\omega}$ decays exponentially as $n \rightarrow \infty$ and $\bar{\Phi} = \hat{\Phi} + \arctan(\lambda/\omega)$. Thus $Z_n \rightarrow 0$ exponentially with n . Substituting (5.9) into (5.4) now yields

$$\alpha = \alpha_n = -\hat{c}A_n^{\delta_E} e^{\hat{r}\beta\lambda/\omega} \cos(\arctan(\lambda/\omega) - n\pi), \quad (5.10)$$

yielding a sequence of α values of alternating sign converging exponentially to zero. Since β is small (5.9) can now be solved to obtain $\beta = \beta_n(\psi)$, where

$$\beta_n = -\hat{k}\psi^2 - \hat{v}A_n\psi + A_n + O(\hat{r}A_n\psi^2 + \hat{v}\psi^3 + \hat{r}A_n^2). \quad (5.11)$$

Thus the curves of side-tangencies in the (α, β) -plane are parametrised by the original ψ coordinate (in Σ_3) and are, at leading order, parabolas with curvature given by $-\hat{k}$. Turning points of these curves relative to the β -direction occur (to leading order) at $\psi^* = -A_n\hat{v}/2\hat{k}$ and $\beta_n^* = A_n$. Substituting into (5.4), we find that at leading order

$$\alpha_n^* = -\hat{c}(\beta_n^*)^{\delta_E} \cos\left(\hat{\Phi} - \frac{\omega}{\mu} \ln \beta_n^*\right),$$

so these points lie on the leading-order curve of tip-tangencies given by equation (5.7).

The higher order terms in (5.7), (5.10) and (5.11) vanish when $\hat{v} = \hat{r} = 0$. In this case the tip-tangency and side-tangency curves are globally connected and the tip-tangency curve reduces to the snaking curve

$$\alpha = -\hat{c}\beta^{\delta_E} \cos\left(\hat{\Phi} - \frac{\omega}{\mu} \ln \beta\right),$$

while the parabolas of side-tangencies collapse onto the vertical half lines

$$\{\alpha = -\hat{c}e^{(\bar{\Phi}-n\pi)\lambda/\omega} \cos(\arctan(\lambda/\omega) - n\pi), \quad \text{sgn}(\beta - e^{(\bar{\Phi}-n\pi)\mu/\omega}) = \text{sgn}(-\hat{k})\},$$

i.e., the turning points of the tip-tangency curve in the α -direction coincide with the turning points of the doubly covered vertical side-tangencies in the β -direction as

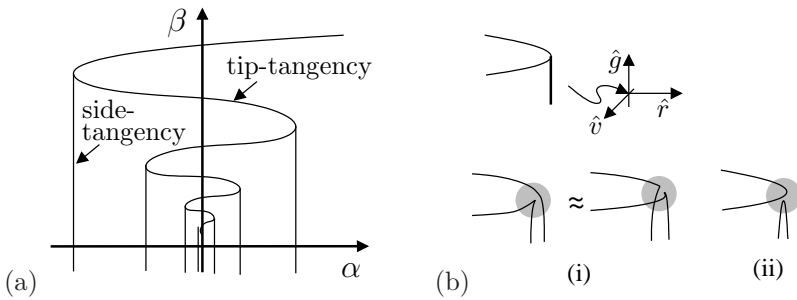


FIG. 5.5. Case III: Sketch of the curves of P -homoclinic tangencies in the case $\hat{k} > 0$. (a) The leading-order geometry, i.e., the special case $\hat{g} = \hat{r} = \hat{v} = 0$. (b) A schematic for the case $\hat{g}, \hat{r}, \hat{v} \neq 0$ showing the possible connections of the different tangency curves. The inset at the top shows the four curves emanating from the crossing point; note that the vertical curve is double. Since two of the four curves coincide in the degenerate case there are only two possible connectivities: (i) tip- to side-tangency, (ii) tip- to tip-tangency and side- to side-tangency. The precise configuration within each of the shaded circles and the values of $\hat{r}, \hat{g}, \hat{v}$ corresponding to each case is beyond the scope of our analytical considerations.

shown in Fig. 5.5(a). Upon perturbing $\hat{g}, \hat{r}, \hat{v}$ away from zero we expect the doubly-covered vertical side-tangency curves and their connections at the turning points to separate (Fig. 5.5(b)). Indeed, direct numerical computation of the condition for double roots of (5.4), shown in Fig. 5.6, corroborates the geometric observation that can be inferred from Fig. 5.2: the two pairs of tangency curves meeting at turning points cross-connect in one smooth curve and one cusp. Specifically, we find that for $\hat{k} > 0$, the outward side-tangency and upper tip-tangency curves form a smooth curve, and the inner side-tangency and lower tip-tangency curves form a cusp. The case $\hat{k} < 0$ creates the same connectivity but with the direction of β reversed (see Fig. 5.6(c)).

We note one curiosity in panel (d) of Fig. 5.6 for the case $k < 0$: the curves of side-tangencies reconnect for large β producing a Calla lily type of structure. This reconnection does not happen for $k > 0$. Presumably this is a consequence of the topological distinction between the spirals $W^u(P) \cap \Sigma_2$ which have infinitely many windings for small positive β when $k < 0$, but only finitely many for positive β when $k > 0$, with this number tending to zero as β increases. However, this behaviour is outside the scope of our local analysis and most likely irrelevant to the unfolding of the bifurcation in question for which we implicitly assume that α and β are small.

In summary, the transition from real to complex eigenvalues does not affect the locations of the heteroclinic connections, cycles and tangencies (these are as shown in Fig. 3.4 for the case $\hat{k} > 0$), nor the location of the E -homoclinics. However, the location of the P -homoclinics is substantially changed. For real eigenvalues the parameter regime for which there are P -homoclinic orbits is bounded by two curves: C_1 , the half of the β -axis where EP1-cycles exist; and C_2 , a curve emanating from the origin and continuing monotonically in α . As the eigenvalues become complex, the analogue to C_2 folds infinitely often about C_1 (so C_2 becomes a snaking curve) with additional, almost-vertical curves of tangencies appearing. Pairs of P -homoclinics are created on each curve of P -homoclinic tangencies, and so there are regions of parameter space in which there are no P -homoclinics, other regions where there are two P -homoclinics, other regions where there are four P -homoclinics, and so on, as illustrated in Fig. 5.6.

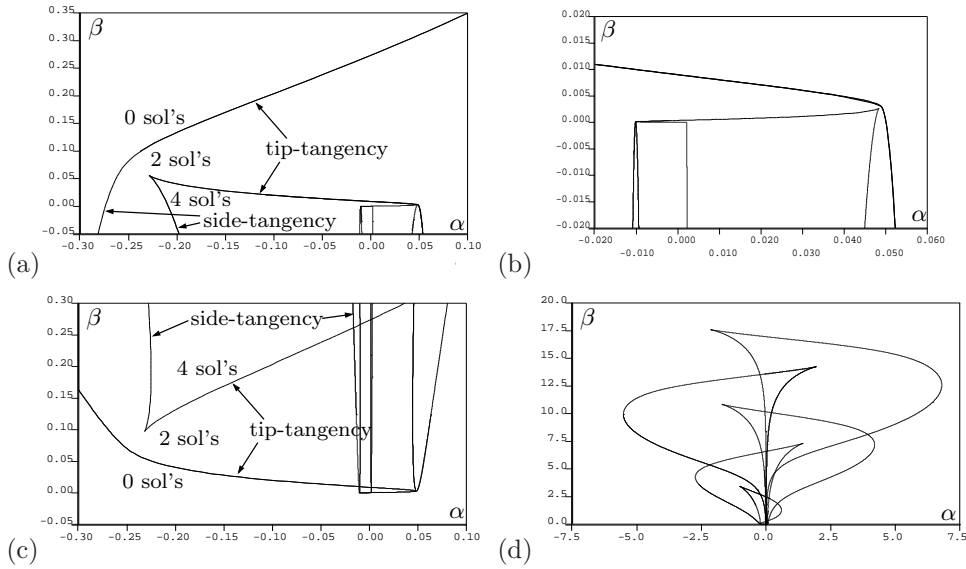


FIG. 5.6. Numerical solutions to the exact P -homoclinic tangency conditions (5.4) and $d\alpha/d\psi = 0$, for $\hat{c} = -1$, $\hat{v} = 1$, $\delta_E = 1/2$, $\omega/\mu = 1$, $\hat{\Phi} = 0$, $\hat{g} = 1$, $\hat{r} = 1$. (a) The case $\hat{k} = 1$. Labelling of tangencies is in terms of the limiting leading-order approximations; numbers refer to relative change in number of P -homoclinic solutions. (b) Magnification of (a). Note how the disconnection between the side and tip tangencies becomes less pronounced as $\alpha, \beta \rightarrow 0$. (c) Similar depiction of the case $\hat{k} = -1$. Panel (d) is the same bifurcation set as in (c) but for a larger range of α and β .

6. Dynamics of the full return map. A complete unfolding of the dynamics in the neighbourhood of an EP1t-point is likely to be highly involved, especially in the case of complex eigenvalues at E satisfying the Shil'nikov condition $\delta_E < 1$. Even in the absence of a P -homoclinic tangency, it is known that near such an equilibrium, shift dynamics occur with respect to arbitrarily many symbols, and the dynamics is nowhere structurally stable, for example, because of arbitrarily close parameter values where multi-pulse E -homoclinics occur [14]. For the P -homoclinic tangencies, so-called wild hyperbolic sets (or Newhouse sinks) necessarily occur at nearby parameter values, with (if $\delta_P < 1$) parameter values with infinitely many stable periodic orbits. See, for example, [27, 12, 10]. The combination of these two kinds of dynamics will be yet more complex.

We focus, therefore, on answering the question of what happens to the simplest folds of *primary* periodic orbits in a neighbourhood of the EP1t-point. By primary, we mean those periodic orbits that form a sequence which converges on the single-pulse E -homoclinic orbits or P -homoclinic tangency. In both cases, where this is an accumulation of folds on the homoclinic orbit in question, there is also an accumulation of period-doubling bifurcations. However, for topological reasons, these period-doublings typically occur very close to the fold bifurcations. See, for example, [13, 11]. So, for simplicity, we do not compute the loci of period-doubling bifurcations in the parameter plane, as, broadly speaking, we can infer this information from knowledge of the location of the folds. We consider positive Floquet multipliers of P only.

6.1. Case I: Real eigenvalues of E , positive Floquet multipliers of P .

In this case, away from the EP1t-point, there are no infinite sequences of folds of

periodic orbits accumulating on the E -homoclinic orbits, so the question becomes: what happens as we approach the EP1t-point to the sequence of folds of periodic orbits known to accumulate on the P -homoclinic tangency?

We start by constructing the full Poincaré map in this case. Specifically we construct the map $R : \Sigma_2 \rightarrow \Sigma_2$, $R \equiv \Pi_1 \circ \Pi_0 \circ \Pi_3 \circ \Pi_2$. Upon combining expressions (3.2), (3.4), (3.5) and (3.6), we obtain

$$\begin{pmatrix} \psi \\ \eta \\ h_2 \end{pmatrix} \mapsto \begin{pmatrix} \tilde{a}Z_n^{\delta_E} + \tilde{b}(\bar{y} + g\Lambda_n + \tilde{q}\eta^{\delta_P} + r\beta)Z_n^{\delta_E} + f\alpha \\ \tilde{c}Z_n^{\delta_E} + \tilde{d}(\bar{y} + g\Lambda_n + \tilde{q}\eta^{\delta_P} + r\beta)Z_n^{\delta_E} + \alpha \\ h_2 \end{pmatrix}, \quad (6.1)$$

where

$$Z_n(\eta, \psi, \beta) = k\Lambda_n^2 - S\eta^{\delta_P} + \beta + v\beta\Lambda_n, \quad \Lambda_n(\eta, \psi) = \Psi + \psi - \frac{\Omega}{m} \ln \eta - 2n\pi.$$

Here the integer n counts the number of complete circuits an orbit makes close to P , $S = -sh_2h_3^{-\delta_P}$ as before, and the various constants with tildes are defined in terms of the original constants as

$$\tilde{a} = ah_0h_1^{-\delta_E}, \quad \tilde{b} = bh_1^{-\delta_E}, \quad \tilde{c} = ch_0h_1^{-\delta_E}, \quad \tilde{d} = dh_1^{-\delta_E}, \quad \tilde{q} = qh_2h_3^{-\delta_P},$$

with $\Psi = (\Omega/m) \ln h_3$. Note, from the construction, that the map is only valid for

$$\eta > 0, \quad \text{and} \quad Z_n > 0.$$

Periodic orbits of the flow correspond to fixed points of map (6.1).

The condition for a fixed point can be considerably simplified by considering only the leading-order terms of (6.1), remembering that $\hat{\delta}_E > \delta_E$ and that the terms being raised to these powers must be small for a fixed point at small α and β to be present. Hence we have the leading-order fixed point conditions:

$$\begin{aligned} \psi &= \tilde{a}Z_n^{\delta_E} + f\alpha, \\ \eta &= \tilde{c}Z_n^{\delta_E} + \alpha. \end{aligned}$$

The second equation can be used to eliminate Z_n from the first equation, resulting in an expression for ψ in terms of η and α . Substituting this into the second equation then gives

$$\eta = \tilde{c}\hat{Z}_n^{\delta_E} + \alpha, \quad \eta, Z_n > 0, \quad (6.2)$$

where

$$\hat{Z}_n(\eta, \alpha, \beta) = k\hat{\Lambda}_n^2 - S\eta^{\delta_P} + \beta + v\beta\hat{\Lambda}_n, \quad \hat{\Lambda}_n(\eta, \alpha) = \Psi + \hat{a}\eta + \tilde{f}\alpha - \frac{\Omega}{m} \ln \eta - 2n\pi,$$

and $\hat{a} = \tilde{a}/\tilde{c}$, $\tilde{f} = f - \tilde{a}/\tilde{c}$.

Fold bifurcations are given by double roots of the fixed point equation for the map (6.1), and hence to leading order by double roots of (6.2). It is instructive to rewrite (6.2) in the form

$$\left(\frac{\eta - \alpha}{\tilde{c}} \right)^{1/\delta_E} = k\hat{\Lambda}_n^2 - S\eta^{\delta_P} + \beta + v\beta\hat{\Lambda}_n, \quad (6.3)$$

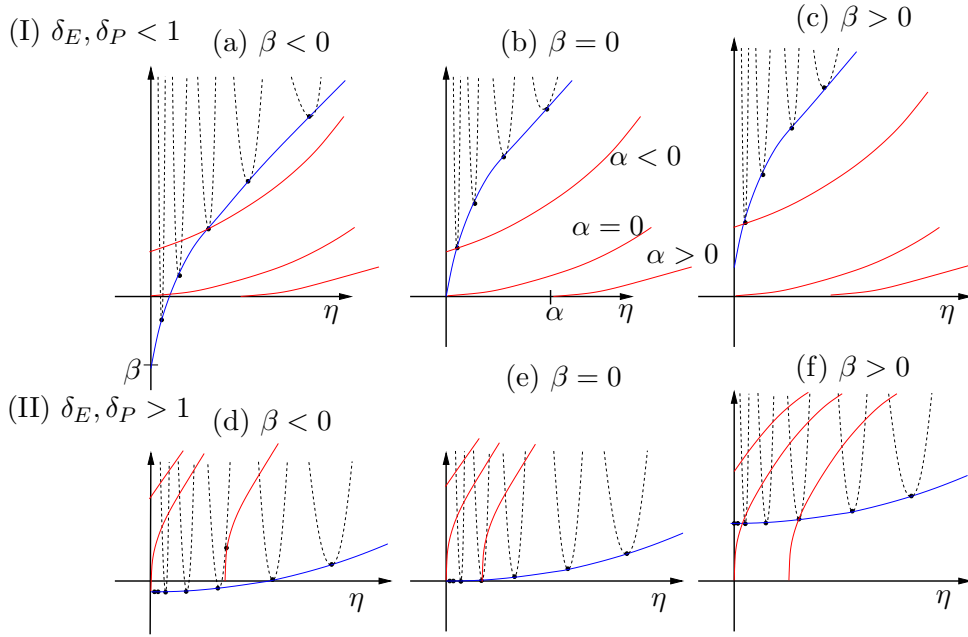


FIG. 6.1. Sketch of the right-hand side of (6.3) for different n (dashed curves) and the envelope as $n \rightarrow \infty$ (solid blue curve); the left-hand side of (6.3) for various values of α (solid red lines) is also shown. Here $\tilde{f} = 0$, $k > 0$, $\tilde{c} > 0$ and $S < 0$. (a)-(c) $\delta_E < 1$, $\delta_P < 1$; (d)-(f) $\delta_E > 1$, $\delta_P > 1$. Intersections between the red curve and dashed lines for positive ordinate and abscissa correspond to fixed points of the return map, and double roots correspond to fold bifurcations. Note that the folds occur at $\eta \approx \eta_n$, where the dashed curve touches its envelope; the latter are indicated by solid circles.

and plot the left- and right-hand sides as η varies. In doing so, we note that the right-hand side has local extrema for $\Lambda_n \approx 0$ (one for each choice of n) and these occur when the right-hand side takes the approximate value $\beta - S\eta^{\delta_P}$.

For now we make the simplification $\tilde{f} = 0$, and consider the case $\delta_E < 1$, $\delta_P < 1$ with the choice $k > 0$, $\tilde{c} > 0$, $S < 0$ as depicted in Fig. 6.1(a)-(c). For $\beta > 0$ fixed there are infinitely many values of α for which the graph of the left-hand side of equation (6.3) (the red curve) is tangent to the graph of the right-hand side (the dashed black curve). These values are fold points, and all occur for negative values of α and converge on the value $\beta = (-\alpha/\tilde{c})^{1/\delta_E}$, which is the condition $\alpha = -\tilde{c}\beta^{\delta_E}$ derived earlier for P -homoclinic tangencies. A tangency between the graphs involving one particular loop of the graph of the right-hand side (i.e., one particular value of n) can be maintained by simultaneously decreasing β while increasing α , and we thus find curves of folds in the second quadrant of the (α, β) -plane accumulating on the curve of P -homoclinic tangencies.

For fixed $\beta < 0$, there are only finitely many tangencies between the two graphs for positive Z_n ; the tangency corresponding to a particular choice of n will persist as β is decreased through zero only until the corresponding loop of the graph of the right-hand side of equation (6.3) first touches the η -axis. This occurs when $\hat{\Lambda}_n \approx 0$, i.e.,

$$\eta_n \approx e^{\frac{m}{\Omega}(\Psi - 2n\pi)},$$

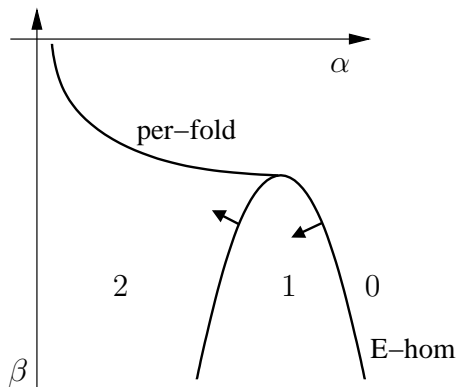


FIG. 6.2. Schematic diagram showing a partial unfolding of the inclination flip bifurcation in the (α, β) -plane. The curve labelled *per-fold* is the locus of a fold of periodic orbits. The arrows indicate the direction of bifurcation of periodic orbits from the E -homoclinic; this direction changes at the point where the fold touches the E -homoclinic curve, i.e., at the inclination flip point. The numbers indicate how many periodic orbits exist in each region of parameter space. Note that the unfolding is partial because there may exist other bifurcations that do not affect our analysis, i.e., multi-pulse homoclinic bifurcations, period-doubling bifurcations, and horseshoe dynamics.

and so the last tangency for this n occurs for $\alpha \approx \eta_n$ ($= \alpha_n$ as defined in §3.2) and $\beta \approx S\eta_n^{\delta_P}$ ($= \beta_n$ as defined in §3.2), i.e., close to the tip of the corresponding parabola of E -homoclinic orbits in the fourth quadrant of the (α, β) -plane (see Fig. 3.5). Numerical solutions of equation (6.2), shown in Fig. 6.3(a), confirm these conclusions: each branch of folds terminates when it reaches the tip of an E -homoclinic parabola. As such a point is approached, $\Lambda_n \rightarrow 0$ and so $Z_n \rightarrow 0$, implying that the period of the periodic orbit undergoing the fold diverges to infinity as it approaches the E -homoclinic bifurcation. The point where the fold and the E -homoclinic touch will thus be a codimension-two point (Fig. 6.2) at which there is a switch in the direction (in parameter space) in which the periodic orbit emerges from the homoclinic orbit. To see that this must occur, note that there are three types of bifurcations of homoclinic orbits that lead generically to this type of *side-switching*. One of these occurs as a result of eigenvalue resonance [5] ($\lambda = \mu$ in our notation), while another is the so-called orbit flip [31] in which the E -homoclinic orbit switches between components of the leading stable eigenvector. The latter cannot happen here owing to our assumptions on the geometry near E . Thus the side-switching must be due to an *inclination flip*. At such a point the stable manifold of E followed (backwards in time) along the E -homoclinic orbit changes between being orientable and non-orientable [18, 19].

There are, in fact, three types of unfolding for the inclination flip bifurcation, depending on the eigenvalues. Following the notation of [17] these are the cases **A** (no other bifurcations), **B** (homoclinic doubling), and **C** (complex dynamics including n -homoclinic and n -periodic orbits for arbitrary values of n and horseshoe dynamics). Case **A** only occurs for $\delta_E > 1$, which is not the case under investigation here. The other two cases occur for $\delta_E < 1$; which of these occurs depends on the value of the non-leading stable eigenvalue. However, both cases feature the fold bifurcation and side switching, and the extra bifurcations do not concern us.

We next consider the case $\delta_E > 1$, $\delta_P > 1$ with the same choice of signs of k , S and \tilde{c} , depicted in Figs 6.1(d)–(f) and 6.3(d). Again, for $\beta > 0$, there are infinitely many values of α for which there are folds, and these converge on $\alpha = -\tilde{c}\beta^{\delta_E}$. However,

in contrast to the previous case, there are now infinitely many tangencies between the two graphs for arbitrarily large $|\beta|$, with $\beta < 0$. This is a consequence of the infinite slope of the left-hand side of (6.3) as a function of η as $\eta - \alpha \rightarrow 0$. This curve can now become tangent to the dashed line at points other than those on the blue envelope where $\eta = \eta_n$. Such a point of tangency, which must occur for $\alpha > 0$, is depicted in Fig. 6.1(d). Note that as $\beta \rightarrow -\infty$ these points occur closer and closer to $Z_n = 0$, and so α becomes closer and closer to the η value at which the right-hand limb of the corresponding dashed curve intersects the η -axis in Fig. 6.1. These are the parameter values for the right-hand part of the parabolic E -homoclinic curves in the (α, β) -plane. Thus each (red) curve of folds hugs closely the right-hand branch of the corresponding (blue) curve of E -homoclinic orbits in Fig. 6.3(d).

The cases $\delta_E < 1$, $\delta_P > 1$ and $\delta_E > 1$, $\delta_P < 1$ can be analyzed similarly. Numerical solutions of equation (6.3) are shown in Fig. 6.3(b) and (c), respectively. Note that the crucial distinction is in the sign of $\delta_E - 1$. If this is positive we find inclination flip points near the tips of the E -homoclinic parabolas, while if it is negative we find persistence of folds to large negative β .

The simplifying assumption $\tilde{f} = 0$ is not, in fact, necessary. In particular, a Taylor expansion with respect to η can be used about each point at which (6.3) has a double root η^* with respect to η to show that a rescaling of α by the multiplicative factor $(1 + \tilde{f}\eta^*m/\Omega)$ leads to an equation that is identical to leading order but with $\tilde{f} = 0$.

We have focused here on the case $k > 0$, $\tilde{c} > 0$, $S < 0$. Cases with different signs of k , \tilde{c} and S can be analyzed similarly.

6.2. Case III: Complex eigenvalues at E , positive Floquet multipliers at P . In contrast to the previous sections, we do not give a rigorous analysis of this case. Instead, we are guided by numerical results and approximate topological arguments.

The full Poincaré map in this case is $\hat{R} : \Sigma_2 \rightarrow \Sigma_2$, $\hat{R} \equiv \Pi_1 \circ \hat{\Pi}_0 \circ \hat{\Pi}_3 \circ \Pi_2$. Composing the maps written down before and using the compound angle formula to simplify the expressions obtained, we find:

$$\begin{pmatrix} \psi \\ \eta \\ h_2 \end{pmatrix} \mapsto \begin{pmatrix} A\bar{Z}_n^{\delta_E} \cos\left(\theta_1 + \hat{g}\Lambda_n + \bar{q}\eta^{\delta_P} + \hat{r}\beta - \frac{\omega}{\mu} \ln \bar{Z}_n\right) + f\alpha \\ C\bar{Z}_n^{\delta_E} \cos\left(\theta_2 + \hat{g}\Lambda_n + \bar{q}\eta^{\delta_P} + \hat{r}\beta - \frac{\omega}{\mu} \ln \bar{Z}_n\right) + \alpha \\ h_2 \end{pmatrix}, \quad (6.4)$$

where

$$\bar{Z}_n(\eta, \psi, \beta) = \hat{k}\Lambda_n^2 - \hat{S}\eta^{\delta_P} + \beta + \hat{v}\beta\Lambda_n, \quad \Lambda_n(\eta, \psi) = \Psi + \psi - \frac{\Omega}{m} \ln \eta - 2n\pi,$$

$$A = h_0 h_1^{-\delta_E} \sqrt{a^2 + b^2}, \quad C = h_0 h_1^{-\delta_E} \sqrt{c^2 + d^2}, \quad \hat{S} = -\hat{s}h_2 h_3^{-\delta_P}, \quad \bar{q} = \hat{q}h_2 h_3^{-\delta_P},$$

$$\theta_1 = \tan^{-1}\left(-\frac{b}{a}\right) + \frac{\omega}{\mu} \ln h_1, \quad \theta_2 = \tan^{-1}\left(-\frac{d}{c}\right) + \frac{\omega}{\mu} \ln h_1,$$

and all other quantities and constants are as defined after equation (6.1). The map is only valid for

$$\eta > 0, \quad \text{and} \quad \bar{Z}_n > 0.$$

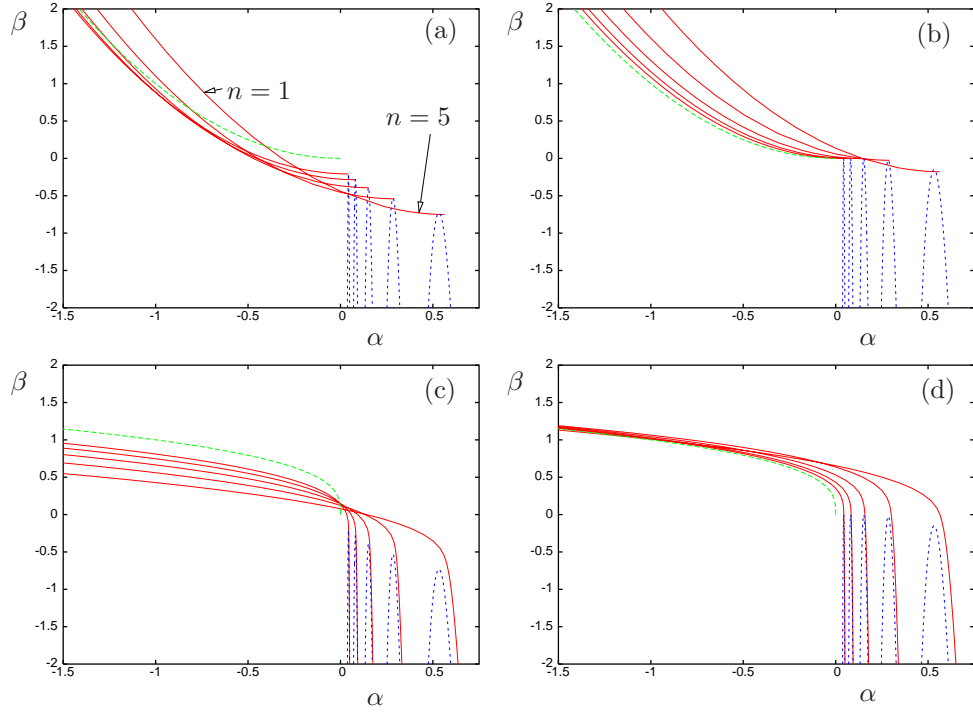


FIG. 6.3. Curves of fold bifurcations of periodic orbits (solid red lines) in the case of real eigenvalues for E , computed using the one-dimensional map (6.2) for $1/\Omega = 0.1$, $\tilde{f} = \hat{a} = 1/2$, $\tilde{c} = 1$, $\tilde{\psi} = 0$, $k = 1$, $S = -1$ and $v = 0$ and (a) $\delta_E = \delta_P = 1/2$, (b) $\delta_E = 1/2$, $\delta_P = 3$, (c) $\delta_E = 3$, $\delta_P = 1/2$, and (d) $\delta_E = \delta_P = 3$. Short (blue) and long (green) dashed lines represent, respectively, the position of E -homoclinic orbits and P -homoclinic tangencies, given by formulae (3.8) and (3.13), respectively.

Equations (6.4) can be simplified slightly by noting that we are interested in solutions with \tilde{Z}_n small, in which case two terms in the argument of each of the cosine terms in the map can be ignored. The simplified map is:

$$\begin{pmatrix} \psi \\ \eta \\ h_2 \end{pmatrix} \mapsto \begin{pmatrix} A\tilde{Z}_n^{\delta_E} \cos\left(\theta_1 + \hat{g}\Lambda_n - \frac{\omega}{\mu} \ln \tilde{Z}_n\right) + f\alpha \\ C\tilde{Z}_n^{\delta_E} \cos\left(\theta_2 + \hat{g}\Lambda_n - \frac{\omega}{\mu} \ln \tilde{Z}_n\right) + \alpha \\ h_2 \end{pmatrix}, \quad (6.5)$$

where

$$\tilde{Z}_n(\eta, \psi, \beta) = \hat{k}\Lambda_n^2 - \hat{S}\eta^{\delta_P} + \beta.$$

We seek double roots of the fixed point equations for this map, which correspond to folds of periodic orbits of the underlying flow. Fig. 6.4 shows a detailed computation of fold points of this two-dimensional map in the (α, β) -plane for the parameter values

$$\begin{aligned} A = 0.5, \quad C = 1, \quad f = 1, \quad \hat{k} = 1, \quad \hat{S} = -1, \quad \delta_P = 3, \\ \theta_1 = 1, \quad \theta_2 = 0, \quad \Psi = 0, \quad \Omega/m = 10, \end{aligned} \quad (6.6)$$

and different choices of the values of the remaining parameters.

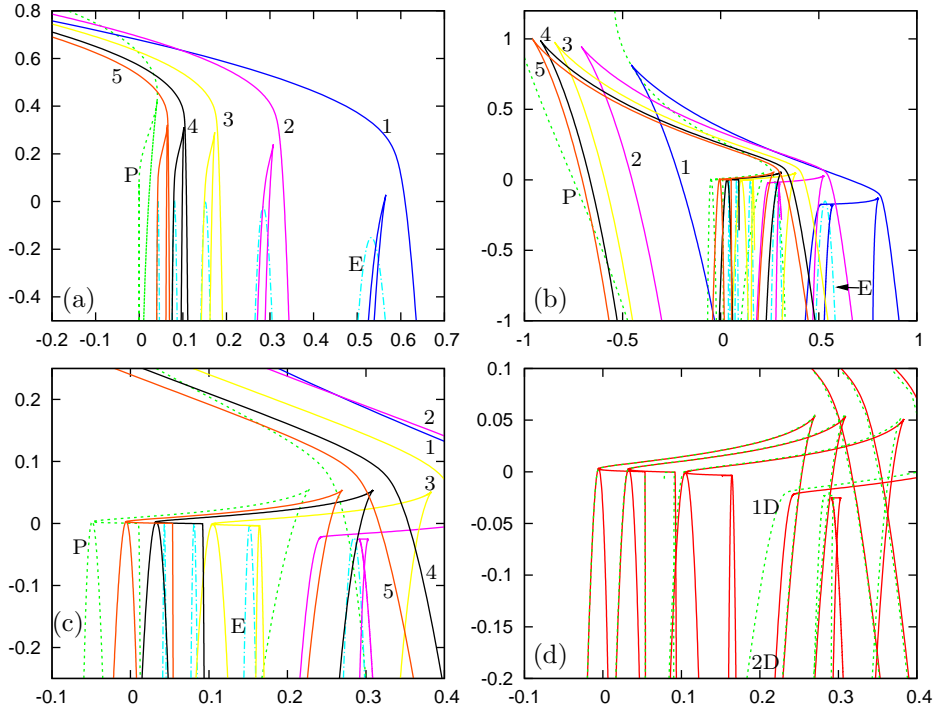


FIG. 6.4. Curves showing fold solutions to the approximate two-dimensional map (6.5) for fixed parameters (6.6) (a) $\hat{g} = 0$, $\omega/\mu = 2$, $\delta_E = 3$; (b) $\hat{g} = 1$, $\omega/\mu = 1$, $\delta_E = 0.5$. Each curve of folds is labelled by the number n of winds near P made by the corresponding periodic orbit. Also plotted in panels a)-(c) are the loci of E -homoclinic orbits (blue dot-dashed curves) and P -homoclinic tangencies (green dotted curves) given by the formulae derived earlier. Panel (c) is a blow-up of (b) and (d) shows the same fold data (in red) plotted together with the corresponding fold curves of the one-dimensional approximation (6.7) to the map.

The main distinction between the first two panels in Fig. 6.4 is the value of δ_E : in panel (a) $\delta_E > 1$ whereas in panel (b) (which is magnified in panel (c)) $\delta_E < 1$. In panel (a), according to the theory of Shil'nikov homoclinic bifurcations [11, 13], each E -homoclinic orbit should be surrounded by at most finitely many fold bifurcations. This is borne out in panel (a), where we see an additional pair of folds joined by a cusp near each curve of E -homoclinics. In contrast, in panel (b) we find strong numerical evidence for infinitely many fold curves near each E -homoclinic locus. Only a few curves (representative consecutive folds along a branch of periodic orbits approaching each E -homoclinic orbit) are shown. Note the presence of additional cusps as well. We have performed other computations of fold curves of these maps for different values of the coefficients. The same broad features are obtained. However the precise location of, for example, the cusp points depends sensitively on the values of various parameters, such as \tilde{c} , \hat{k} , \hat{S} and \hat{g} .

In order to explain the characteristic shape of these fold curves and the presence of cusps on them, it is tempting to try to reduce (6.5) to a one-dimensional fixed point equation, just as we did in the case of real eigenvalues to produce (6.2). In that case, simple algebraic manipulation led to the elimination of ψ . However, this approach does not work here unless $\theta_1 = \theta_2$ since the two cosine terms in (6.4)

have different arguments. On the other hand if one supposes that ψ must be small compared to $\frac{\Omega}{m} \ln \eta$ in the expression for Λ_n one is led to looking at fixed points of the one-dimensional map

$$\eta \mapsto C \tilde{Z}_n^{\delta_E} \cos \left(\theta_2 + \hat{g} \Lambda_n - \frac{\omega}{\mu} \ln \tilde{Z}_n \right) + \alpha, \quad (6.7)$$

where all terms are defined as before except for

$$\Lambda_n(\eta) \equiv \tilde{\psi} - \frac{\Omega}{m} \ln \eta - 2n\pi.$$

A similar argument suggests that the term $\hat{g} \Lambda_n$ is then also small compared with $\frac{\omega}{\mu} \ln \tilde{Z}_n$, and hence can also be ignored to leading order. With these assumptions, folds correspond to double roots of the fixed point equation

$$\eta = C \tilde{Z}_n^{\delta_E} \cos \left(\theta_2 - \frac{\omega}{\mu} \ln \tilde{Z}_n \right) + \alpha. \quad (6.8)$$

Note the similarity of (6.8) to the corresponding fixed point equation (6.2) in the real eigenvalue case. In particular, the right-hand side of (6.8) is a rapidly oscillating function of η whose envelope is identical (up to definition of the constants) to the right-hand side of (6.2). This suggests that along curves of folds of the one-dimensional map in the real eigenvalue case we should see ‘folds of folds’ in this complex eigenvalue case; in other words, cusps.

Unfortunately, all attempts to make the argument in the previous paragraph rigorous have proved unsuccessful, and it appears that (6.5) is really a fully-coupled two-dimensional map, much as in the case of a homoclinic orbit to a bifocus [9]. Nevertheless, numerically we find remarkably close agreement between the fold curves obtained by looking for fixed points of the two-dimensional map (6.5) and the folds of the approximate one-dimensional fixed point equation (6.8), as demonstrated in Fig. 6.4(d).

7. Homoclinic snaking and global connections of EP1t-cycles. In applications, we frequently find in two-parameter continuations that E -homoclinic orbits occur along a wide snaking curve like that shown in Fig. 7.3(d); it appears that the E -homoclinic orbits are accumulating on a pair of EP1t-points and on a curve in parameter space joining these points. In this section we give a geometric explanation for this phenomenon based on certain global extensions of our Poincaré map. Our approximate arguments are similar in spirit to the recent rigorous analysis by Beck et al. [2] for homoclinic snaking in the context of reversible systems, which has one codimension less.

We extend the model from the previous sections by making assumptions about properties of the heteroclinic connections from P to E as a parameter is varied over an $O(1)$ interval, and about the ways in which the maps Π_j behave over this interval. We start by noting that in applications heteroclinic connections from P to E typically come in pairs: a pair is created at a tangency between $W^u(P)$ and $W^s(E)$, the two connections persist for an interval of some parameter, and then annihilate pairwise at a second heteroclinic tangency. If a second parameter can be tuned to select values at which codimension-one connections from E to P simultaneously exist, then we will get a curve of EP1 cycles in two-parameter space, with end points of the curve being EP1t-points. Fig. 7.1 shows schematically how this might occur if we extend the parameters α and β , which locally unfold an EP1t-point, to global values.

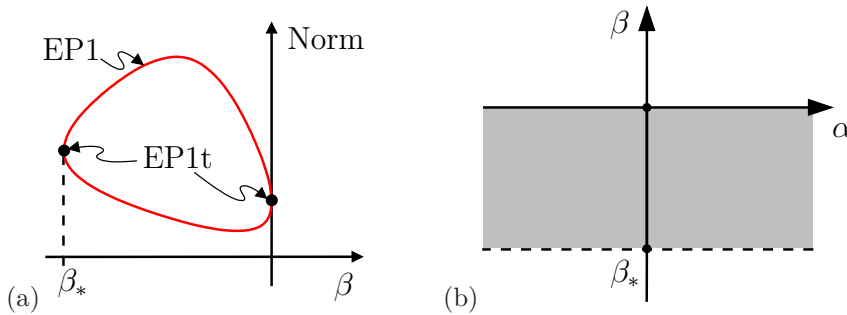


FIG. 7.1. (a) Sketch of a possible bifurcation diagram for connected EP1-cycles; large dots correspond to EP1t-cycles. (b) A possible extension of the situation in (a) to two parameters. In the shaded region there exist two different heteroclinic connections from P to E , with tangencies occurring on the dashed line and the α -axis. Assuming a codimension-one connection from E to P exists for $\alpha = 0$, there will be two distinct EP1-cycles for parameter values on the β -axis with $\beta^* < \beta < 0$.

Since we strive for a simple geometric explanation, we make the following assumptions. We assume that two EP1t-points exist, at (α, β) equal to $(0, 0)$ and $(0, \beta^*)$, where $\beta^* < 0$, and that EP1-cycles occur at points on the β -axis between these two points so that we have the situation shown in Fig. 7.1. We further assume that P and E and their linearizations remain unchanged in an $O(1)$ parameter region containing this interval of EP1-cycles, as does the connection from E to P . Thus the maps Π_j , $j = 0, 1, 2$ will remain valid and unchanged over this $O(1)$ region. It is convenient to work with a cross-section, Σ_3^{glob} , instead of Σ_3 , where Σ_3^{glob} is defined near all phases of P rather than near just one specified phase. We can then derive a new map, $\Pi_{3,\beta}^{\text{glob}} : \Sigma_3^{\text{glob}} \rightarrow \Sigma_0$ that varies globally with β in a simple way, as specified below. In the following, by $W_\beta^s(E)$, we mean the $(\beta$ -dependent) curve of intersections of $W^s(E)$ with Σ_3^{glob} if we run time backwards, i.e., $W_\beta^s(E) = (\Pi_{3,\beta}^{\text{glob}})^{-1} \{(h_0, y, 0)\}$. By $W_\alpha^u(E)$ we mean the curve on Σ_3^{glob} traced out by the point of first intersection of $W^u(E)$ with Σ_3^{glob} as α is varied (see Fig. 7.3).

7.1. Positive Floquet multipliers at P . Using local coordinates near P as described in §3, we define:

$$\Sigma_3^{\text{glob}} = \{(\psi, \eta, \xi) \mid \eta = h_3, 0 \leq \psi < 2\pi\}.$$

In Fig. 7.2, we show schematically the simplest possible geometries of $W^u(P)$ and $W^s(E)$ where they intersect Σ_0 and Σ_3^{glob} , for a β -value for which two EP1t-cycles exist. We assume that to leading order, the only effect of changing parameter β is to move $W_\beta^s(E)$ rigidly up (for an increase in β) or down (when β decreases) so that the two EP1t-cycles occur, respectively, when the points b and d on $W^u(P)$ are simultaneously on $W^s(E)$. For simplicity, we assume that $W_\beta^s(E)$ is sinusoidal in shape, but in fact any smooth periodic function with a single maximum and a single minimum will lead to the same result.

To find E -homoclinic orbits, we need to locate $W^u(E)$ on Σ_3^{glob} . Using maps Π_1 and Π_2 , we compute $W^u(E) \cap \Sigma_3^{\text{glob}}$ to be at (ψ, h_3, ξ) with

$$\psi = \left(\Psi - \frac{\Omega}{m} \ln \alpha \right) \bmod 2\pi, \quad \xi = \tilde{h} \alpha^{\delta_P},$$

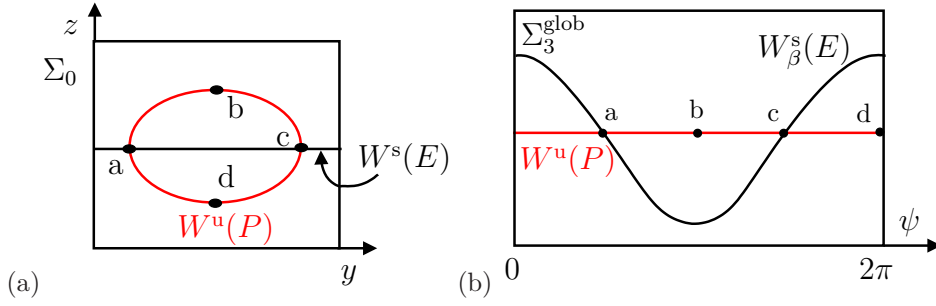


FIG. 7.2. Geometry of $W^u(P)$ and $W^s(E)$ on (a) Σ_0 , (b) Σ_3^{glob} , when two EP1-cycles are present.

to lowest order, where $\tilde{h} = h_2 h_3^{-\delta_P}$. As α varies, this point traces out $W_\alpha^u(E)$, which is a sequence of near horizontal lines converging on $W^u(P)$, as shown in Fig. 7.3(a)-(c). E -homoclinics occur when $W_\alpha^u(E)$ intersects $W_\beta^s(E)$. Since by assumption the position of the former does not depend on β while the latter does not depend on α , the shape of the locus of E -homoclinics can now be deduced, as follows. We start with α and β values for which there is an E -homoclinic orbit (as indicated by the large dot in panel (a) of Fig. 7.3(a)), and decrease α monotonically (which moves the tracer point to the right), while simultaneously varying β to maintain the E -homoclinic orbit. Initially, the E -homoclinic orbit can be maintained by increasing β , which shifts the sinusoidal curve up. However, once β is sufficiently large that the local minimum of $W_\beta^s(E)$ rises too high (this will occur for $\beta \approx 0$, which is the case shown in Fig. 7.3(b)) then β must be decreased to maintain the E -homoclinic orbit. A further small decrease in α can then be compensated for by decreasing β further, at least until the local maximum of $W_\beta^s(E)$ falls too low (for $\beta \approx \beta^*$, as in Fig. 7.3(c)), in which case an increase in β will again be required for maintenance of the E -homoclinic orbit. This process repeats, and we end up with the wide snaking curve shown in Fig. 7.3(d). A similar argument was used in [3] where a snaking curve of E -homoclinic orbits, lying in an exponentially thin wedge, was found in the neighbourhood of a local codimension-two saddle-node/Hopf bifurcation point.

More formally, our global assumptions imply that $W_\beta^s(E)$ is a graph $F_\beta(\psi) : \mathbb{R} \rightarrow \mathbb{R}$ with $F_\beta(\psi + 2\pi) = F_\beta(\psi)$ and $F_\beta(\psi) = F_0(\psi) + G(\beta)$ with monotone G . On the other hand $W_\alpha^u(E)$ is a parametrised curve in Σ_3^{glob} ,

$$\alpha \mapsto \left(\left(\Psi - \frac{\Omega}{m} \ln \alpha \right) \bmod 2\pi, \tilde{h} \alpha^{\delta_P} \right).$$

E -homoclinic orbits occur whenever these curves meet, i.e., when

$$\psi = \left(\Psi - \frac{\Omega}{m} \ln \alpha \right) \bmod 2\pi \quad \text{and} \quad F_\beta(\psi) = \tilde{h} \alpha^{\delta_P}$$

which implies that

$$\beta = G^{-1} \left(\tilde{h} \alpha^{\delta_P} + F_0 \left(\Psi - \frac{\Omega}{m} \ln \alpha \right) \right).$$

Turning points in the E -homoclinic locus arise for α values for which

$$F_0' \left(\Psi - \frac{\Omega}{m} \ln \alpha \right) = 0,$$

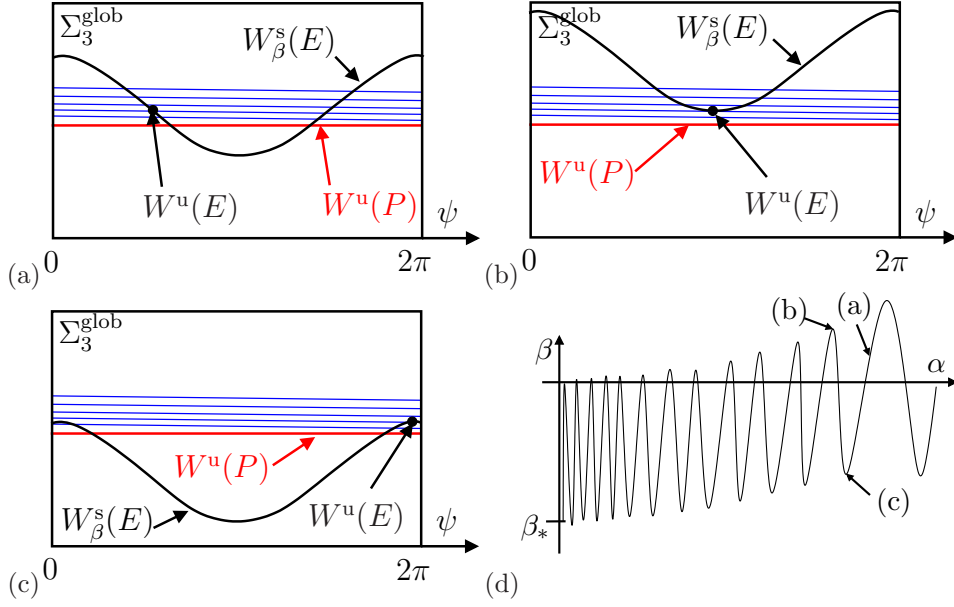


FIG. 7.3. Geometric explanation for the snaking E -homoclinic locus. $W^u(E)$ moves monotonically to larger ψ as α decreases, tracing out the near-horizontal lines, while $W^s(E)$ is shifted monotonically up as β increases. (a) Intersection of $W^u(E)$ and $W^s(E)$ at a value of β such as that indicated by label (a) in panel (d). (b) $W^u(E)$ intersects $W^s(E)$ at its local minimum for $\beta \approx 0$. (c) $W^u(E)$ intersects $W^s(E)$ at its local maximum for $\beta \approx \beta_*$. (d) The corresponding E -homoclinic locus for the case $S > 0$. By assumption, $k < 0$ for the ‘lower’ EP1t-cycle and $k > 0$ for the ‘upper’ (cf. Fig. 3.5). Labels indicate typical parameter values for the situations shown in the corresponding panels.

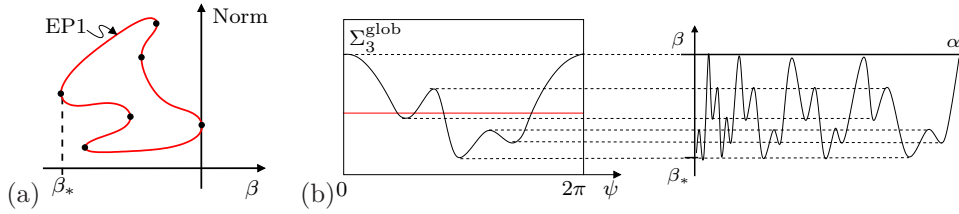


FIG. 7.4. (a) Sketch of a possible bifurcation diagram in the case of six cyclically connected EP1t-points (represented by large dots). (b) Analogue of Fig. 7.2(b) for case (a) traced counter-clockwise, showing the correspondence between the folds in the multi-snaking E -homoclinic locus and the critical points of F_0 . For simplicity, we do not show the geometry of the envelope of fold points in detail (cf. Fig. 3.5.)

i.e., near EP1t-cycles, as computed in §3.

The case discussed above occurs when there are two critical points for F , but there may in fact be more (which would imply more than two connected EP1t-points). For instance, a case with six EP1t-points is shown schematically in Fig. 7.4, and will be discussed further in §8.

7.2. Negative Floquet multipliers at P . In §4 we found that the main effect of negative Floquet multipliers at P on the locus of E -homoclinic orbits was the simultaneous sign change of α and β at successive turning points, with the result

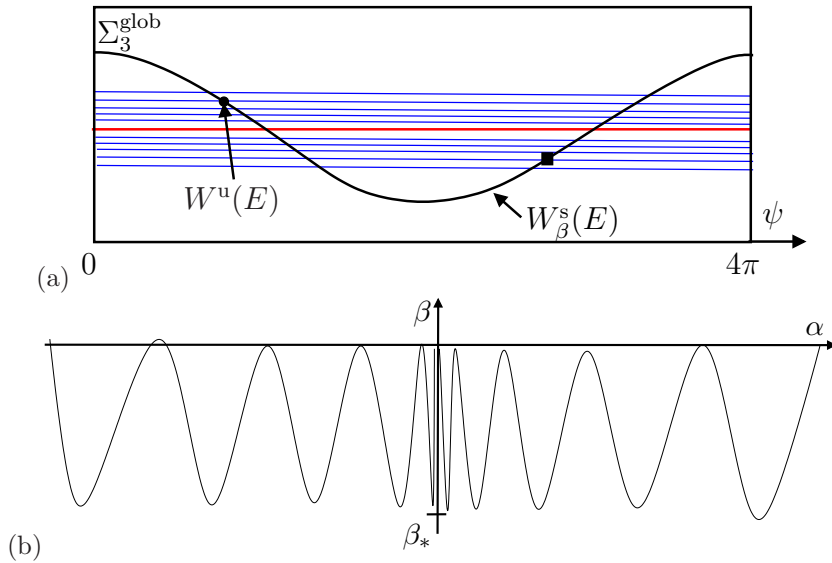


FIG. 7.5. (a) The analogue of Fig. 7.3(a) for negative Floquet multipliers. The large dot shows the intersection of $W^u(E)$ with Σ_3^{glob} for a typical positive value of α . The large square shows the same thing, but for negative α . (b) The corresponding loci of E -homoclinic orbits. For simplicity, we do not show the geometry of the envelope of fold points in detail (cf. Fig. 4.2.)

that half the turning points accumulate on the EP1t-point from positive α and half accumulate from negative α (see Fig. 4.2). The effect of negative Floquet multipliers on the snaking curve is analogous: there are now two snaking curves, accumulating on the interval of EP1-cycles from opposite sides of $\alpha = 0$.

To see this, we first define an alternative version of Σ_3^{glob} appropriate to this case:

$$\Sigma_3^{\text{glob}} = \{(\psi, \eta, \xi) \mid \eta = h_3, 0 \leq \psi < 4\pi\}.$$

This is a double cover of all phases of P ; the need for this form of cross-section is as discussed in §4. Proceeding as before, we again assume that $W_\beta^s(E)$ is a continuous graph with at least two critical points, as shown in Fig. 7.5(a), while β moves it rigidly up or down. As argued in §4, an E -homoclinic occurring near a turning point close to one of the EP1t-points will cross Σ_3^{glob} with ξ positive (resp. negative) if α is positive (resp. negative) at the turning point. Thus $W_\alpha^u(E)$ now has two disjoint components, each consisting of a sequence of near-horizontal lines accumulating on $W^s(P) \cap \Sigma_3^{\text{glob}}$, one with $\xi > 0$ and the other with $\xi < 0$. Arguing as in the previous subsection for each component separately, we deduce that the locus of E -homoclinic orbits consists of two wide snaking curves as described above, and shown in Fig. 7.5. The mechanism leading to the bifurcation of *two* snaking curves for this case is similar to the mechanism operating near E -homoclinic bifurcations from codimension-two equilibrium-to-periodic orbit heteroclinic cycles with winding number two, as described in [28]: these cycles require a phase space of at least four dimensions and occur when the E -to- P connection is itself of codimension two.

8. Numerical examples. EP1t-points have been seen in various systems of ordinary differential equations. A straightforward way to identify the EP1 phenomenon is via E -homoclinics. If homoclinic snaking or an accumulation of folds

of E -homoclinic curves is seen in the bifurcation set for a particular system, then we can diagnose the presence of the EP1 phenomenon by looking at phase portraits along the E -homoclinic curves using standard software such as AUTO and HomCont [6]; an E -homoclinic orbit will pick up extra loops near a periodic orbit and in fact seem to converge to a periodic orbit as it gets close to a presumed EP1t-point. It is also possible to find EP1t-points by continuing curves of P -homoclinic tangencies, heteroclinic connections from E to P , and heteroclinic tangencies from P to E , but this involves the use of more complex software currently under development. See [7, 8, 21].

In §8.1, we describe a system originally designed to model a saddle-node Hopf bifurcation with global reinjection [20]. The bifurcation set for this system contains a snaking E -homoclinic curve that converges in parameter space to a segment connecting two EP1t-points. We show that the rate at which E -homoclinic folds accumulate is consistent with the theory in §5, and that the bifurcation set has a structure of fold bifurcations and cusps that matches the predictions of §6. In §8.2, we discuss a nine-dimensional model of intracellular calcium dynamics [34, 35]. The bifurcation set for this system also contains a snaking E -homoclinic curve, but there are now six EP1t-points involved, as in Fig. 7.4.

Another example is provided by the FitzHugh-Nagumo (FHN) equations, where we do not see a homoclinic snake, but instead a sequence of folded curves of E -homoclinics that are not globally connected in the parameter space. Numerics suggest there exist folds of periodic orbits accumulating on the E -homoclinic orbits and folds accumulating on a P -homoclinic tangency, with the two families of folds being connected via cusps. Since the numerical evidence is not as clear here as for the previous two examples and for reasons of brevity we do not discuss these equations further here but refer the reader to the discussion in [4].

The first of our example systems (saddle-node Hopf model) and the FitzHugh-Nagumo equations contain instances of Case III EP1t-points: complex eigenvalues at E and positive Floquet multipliers at P . The model of calcium dynamics is too stiff for AUTO to be able to calculate Floquet multipliers reliably and so we are unable to determine which case we have. However, in this example, we have at least one EP1t-point at which the leading eigenvalue at E is real and at least one EP1t-point at which there is a complex conjugate pair of leading eigenvalues at E .

8.1. A model from the study of semiconductor lasers. Motivated by studies of semiconductor lasers with optical reinjection, the following system of equations was proposed in [20] as a model of a saddle-node Hopf bifurcation with global reinjection:

$$\begin{aligned}\dot{x} &= \nu_1 x - y + x \sin \varphi - (x^2 + y^2)x + 0.01(2 \cos \varphi + \nu_2)^2 \\ \dot{y} &= \nu_1 y + x + y \sin \varphi - (x^2 + y^2)y + 0.01\pi(2 \cos \varphi + \nu_2)^2 \\ \dot{\varphi} &= \nu_2 - (x^2 + y^2) + 2 \cos \varphi.\end{aligned}\tag{8.1}$$

The bifurcation parameters for this vector field are ν_1 and ν_2 . The system reduces to a standard normal form for a saddle-node Hopf (SNH) bifurcation if a Taylor expansion is performed up to third order at the points $(x, y, \varphi) = (0, 0, 0)$ at $(\nu_1, \nu_2) = (0, -2)$ and $(0, 0, \pi)$ at $(0, 2)$. However, the variable φ is periodic, which causes reinjection and the existence of new orbits, which wind around a cylinder, that would not be present if φ were not periodic.

It was shown in [20] that there exists a curve of E -homoclinic orbits to an equilibrium, b , that emanates from a non-central saddle-node homoclinic bifurcation point

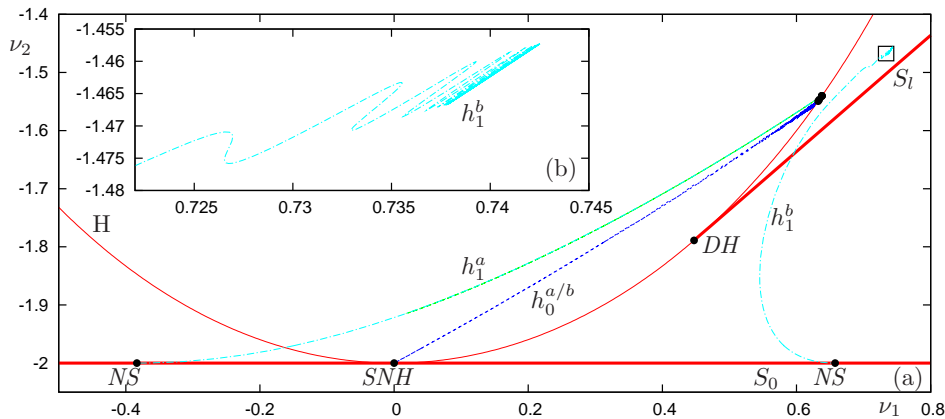


FIG. 8.1. (a) Parameter space overview for system (8.1). The bifurcation curves S_0 (saddle-node of equilibria), H (Hopf), and $h_0^{a/b}$ (two E -homoclinic orbits) emanate from the codimension-two saddle-node Hopf bifurcation SNH . The curve of saddle-node bifurcations of limit-cycles S_l emanates from the degenerate Hopf point DH on the curve H , and the two curves of E -homoclinics, h_1^a and h_1^b , emanate from non-central saddle-node homoclinic bifurcation points NS on S_0 . Panel (b) shows a magnification of the part of parameter space in which the curve h_1^b terminates.

NS ; this curve of E -homoclinics is labelled h_1^b in Fig. 8.1. Panel (b) of that figure shows how h_1^b snakes towards a segment connecting two EP1t-points. The eigenvalues of the equilibrium b at the two EP1t-points are approximately -1.360 and $1.418 \pm i$ at $(\nu_1, \nu_2) = (0.737858, -1.46667)$, and -1.370 and $1.427 \pm i$ at $(\nu_1, \nu_2) = (0.742520, -1.45729)$. The Floquet multipliers of the periodic orbit Γ are 1 , 0.4994 , and 0.526×10^3 at the left-hand EP1t-point and 1 , 0.4980 , and 0.636×10^3 at the right-hand point. Thus both EP1t-points conform to Case III of our analysis. Note that the complex eigenvalues of the equilibrium are reversed in sign with respect to the assumptions made in our analysis, so we need to reverse time to compare with the theory.

This system was investigated further in [21] and additional bifurcation curves were computed, including c_b , the locus of a heteroclinic orbit connecting Γ to b , t_b , the locus of heteroclinic tangencies of $W^u(b)$ and $W^s(\Gamma)$, and t_Γ , a curve of P -homoclinic tangencies. It was shown in [21] that the curves t_b form the approximate envelope of the E -homoclinic curve h_1^b ; the turning points of h_1^b are all approximately on the curves t_b and accumulate on t_b extremely quickly. Ref. [21] also showed that the curve c_b^* , which is the locus of a second heteroclinic orbit connecting Γ to b , accumulates in a way similar to the E -homoclinic curve, snaking between two P -homoclinic tangency curves, t_Γ , and accumulating on a segment of the curve c_b .

In order to compare this model with the theoretical results obtained in §§3.2, 6.2, and 7.1, we apply a linear transformation to parameter space. This is possible because from [21] we know that both the EP1 segment connecting the two EP1t-points and the curves t_b between which the E -homoclinic curve snakes are linear up to numerical accuracy. The linear(-affine) map we use has the form

$$\begin{pmatrix} \mu_1 \\ \mu_2 \end{pmatrix} = \begin{pmatrix} a & b \\ c & d \end{pmatrix} \begin{pmatrix} \nu_1 \\ \nu_2 \end{pmatrix} + \begin{pmatrix} f \\ g \end{pmatrix}, \quad (8.2)$$

where the coefficients a , b , c , d , f , and g are determined by specifying the image of

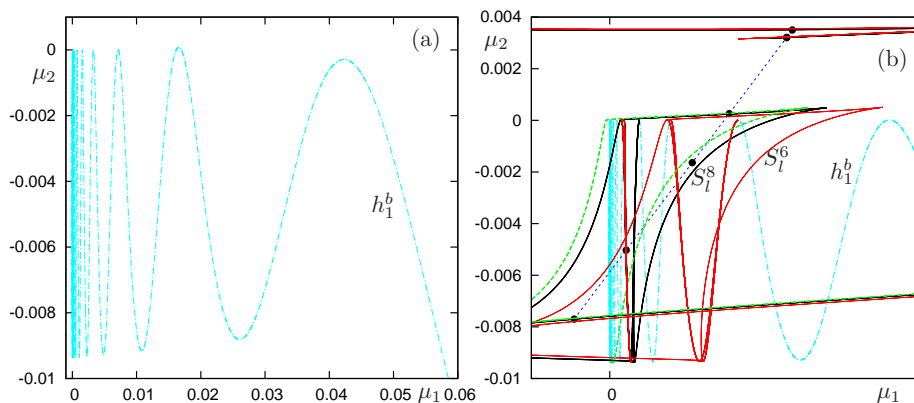


FIG. 8.2. Fig. 8.1(b) after linear mapping of the parameter space as defined by (8.2): (a) the transformed homoclinic snake; (b) the snake with curves of folds of limit cycles (labelled S_l^n) superimposed. Here n denotes the number of loops the associated periodic orbit makes in the vicinity of the orbit Γ . The dashed blue line in panel (b) indicates the path in parameter space used in constructing Fig. 8.5. The large dots on this line show the accumulation points for the folds of the periodic orbit shown in Fig. 8.5(a).

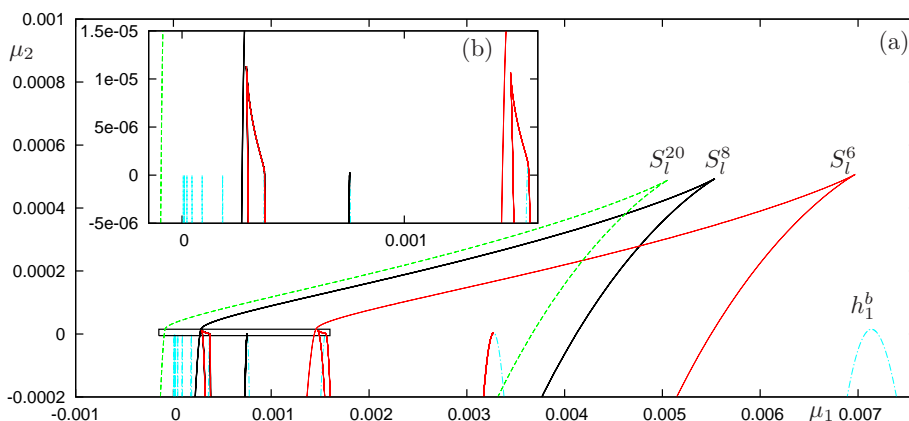


FIG. 8.3. (a) Blow-up of Fig. 8.2(b) around $\mu_2 = 0$. (b) Blow-up of the boxed area around $(0, 0)$ in panel (a).

three points: the two EP1t-points are mapped to the μ_2 -axis (specifically, to $(0, 0)$ and approximately $(0, -9.4 \times 10^{-3})$) and one of the (relatively high order) turning points of the homoclinic snake is mapped to the μ_1 -axis (specifically, the turning point called q_9 in Table 8.1, which lies very close to heteroclinic tangency t_b , is mapped to the point $(\mu_1, \mu_2 \approx (5.5 \times 10^{-6}, 0))$). These requirements result in approximate values of the constants $a = -1.73$, $b = 0.859$, $c = -1.46$, $d = 1.73$, $f = 2.54$, $g = 3.61$. Applying this mapping yields Fig. 8.2 which shows the E -homoclinic in the new coordinate frame; panel (a) shows the transformed snake alone and panel (b) shows the snake with some curves of folds of limit cycles superimposed.

In this new coordinate frame it is straightforward to extract the horizontal scaling law for the E -homoclinic snake. The theory for this case (case III) predicts that the scale factor by which the μ_1 -coordinate of successive turning points reduces is

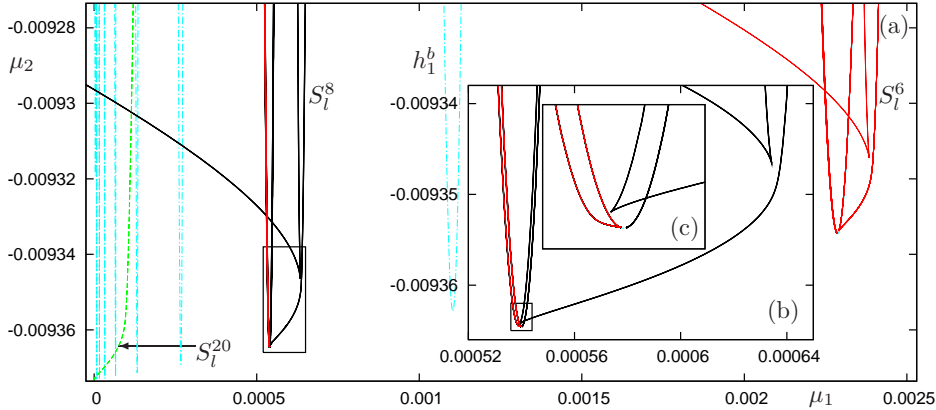


FIG. 8.4. (a) Blow-up of Fig. 8.2(b) around $\mu_2 = -0.0093$. (b) Blow-up of the boxed area around $(0.0006, -0.00935)$ in panel (a). (c) Further blow-up of the boxed area in panel (b). The dashed blue line in panel (a) indicates the path in parameter space used in constructing Fig. 8.5.

equal to the stable Floquet multiplier, i.e., 0.4994 for the minima and 0.4980 for the maxima. As summarised in Table 8.1, the horizontal scaling of the homoclinic snake matches this prediction up to almost four decimal places. Due to more accurate calculations, this gives an improvement in numerical accuracy of almost two decimal places compared with the results of [20]. It is not possible to extract accurate estimates of the vertical scaling from this data: the vertical scale factor is predicted to be equal to the reciprocal of the unstable Floquet multiplier, i.e., more than 200 times smaller than the horizontal scale factor, and appears to be dwarfed by higher-order effects. Figs 8.3 and 8.4 show magnifications of the top and bottom parts of Fig. 8.2(b), in particular showing the folds of limit cycles. Notice the striking similarity with Fig. 6.4.

Finally, we show numerical evidence for the existence of P -homoclinic tangencies near the purported EP1t-points. Following the periodic orbit S_l^8 along the path in parameter space indicated by the dashed blue line in Figs 8.2 yields the bifurcation diagram in Fig. 8.5(a). It can be seen that the periodic orbit emanates from an E -homoclinic bifurcation at $\nu_2 \approx -1.463$, passes through a lot of folds, and eventually appears to approach some P -homoclinic tangencies (presumably one tangency corresponding to each accumulation point of folds of the periodic orbit). Fig. 8.5(b) shows phase space pictures at one of the fold bifurcations of lower order. Here, we use a more convenient representation of global periodic and homoclinic orbits in \mathbb{R}^3 , so that it is immediately clear how they close up, as in [20]. This representation was achieved by mapping the φ -axis onto a circle with sufficiently large radius, $R = 2$, using the transformation

$$\begin{aligned} u &= (R + x) \cos \varphi \\ v &= (R + x) \sin \varphi \\ w &= y. \end{aligned}$$

Ref. [4] shows a picture similar to Fig. 8.5 but for the FitzHugh-Nagumo equations.

8.2. A model of intracellular calcium dynamics. The equations we consider in this subsection are travelling wave equations derived from a model for calcium wave

Minima on curve h_1^b :

Point p_i	$\mu_1(p_i)$	$\mu_2(p_i)$	$\delta_i(\mu_1)$	$\delta_i(\mu_2)$
p_1	$2.3250947336 \times 10^{-3}$	$-9.2964538119 \times 10^{-3}$		
p_2	$1.1113889215 \times 10^{-3}$	$-9.3468163580 \times 10^{-3}$		
p_3	$5.4190197325 \times 10^{-4}$	$-9.3626660243 \times 10^{-3}$	0.4692	0.3147
p_4	$2.6706866959 \times 10^{-4}$	$-9.3686543262 \times 10^{-3}$	0.4826	0.3778
p_5	$1.3239903424 \times 10^{-4}$	$-9.3712095355 \times 10^{-3}$	0.4900	0.4267
p_6	$6.5850910620 \times 10^{-5}$	$-9.3723821246 \times 10^{-3}$	0.4942	0.4589
p_7	$3.2810446805 \times 10^{-5}$	$-9.3729424933 \times 10^{-3}$	0.4965	0.4779
p_8	$1.6363181270 \times 10^{-5}$	$-9.3732161068 \times 10^{-3}$	0.4978	0.4883
p_9	$8.1640088701 \times 10^{-6}$	$-9.3733511728 \times 10^{-3}$	0.4985	0.4946

Maxima on curve h_1^b :

Point q_i	$\mu_1(q_i)$	$\mu_2(q_i)$	$\Delta_i(\mu_1)$	$\Delta_i(\mu_2)$
q_1	$1.5441614595 \times 10^{-3}$	$-1.1008437384 \times 10^{-5}$		
q_2	$7.5158021016 \times 10^{-4}$	$-2.4937897816 \times 10^{-6}$		
q_3	$3.6926819386 \times 10^{-4}$	$-5.8516346851 \times 10^{-7}$	0.4824	0.2242
q_4	$1.8246714325 \times 10^{-4}$	$-1.3982899258 \times 10^{-7}$	0.4886	0.2333
q_5	$9.0466481392 \times 10^{-5}$	$-3.3618422283 \times 10^{-8}$	0.4925	0.2385
q_6	$4.4940168388 \times 10^{-5}$	$-8.0767046960 \times 10^{-9}$	0.4948	0.2405
q_7	$2.2349153804 \times 10^{-5}$	$-1.9906733630 \times 10^{-9}$	0.4962	0.2383
q_8	$1.1121307124 \times 10^{-5}$	$-5.7585064323 \times 10^{-10}$	0.4970	0.2325
q_9	$5.5360633840 \times 10^{-6}$	0.0000000000	0.4974	0.4070

TABLE 8.1

Table of scalings for turning points of the E -homoclinic snake in system (8.1). Here, $\delta_i(\mu_j) = |((\mu_j(p_i) - \mu_j(p_{i-1})) / ((\mu_j(p_{i-1}) - \mu_j(p_{i-2})))|$, $\Delta_i(\mu_j) = |((\mu_j(q_i) - \mu_j(q_{i-1})) / ((\mu_j(q_{i-1}) - \mu_j(q_{i-2})))|$, for $j = 1, 2$. For the minima, the computed values of the Floquet multipliers predict a horizontal scale factor of 0.4994 (cf. $\delta_i(\mu_1)$). For the maxima, a horizontal scale factor of 0.4980 is predicted (cf. $\Delta_i(\mu_1)$). The vertical scale factors cannot be extracted accurately from this data.

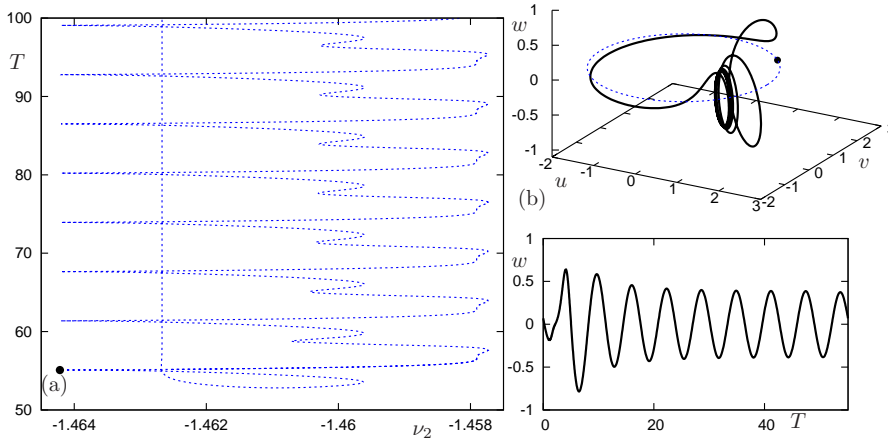


FIG. 8.5. (a) Transition of the periodic orbit S_1^S between an E -homoclinic bifurcation and a pair of P -homoclinic tangencies along the path through parameter space indicated by the dashed blue line in Fig. 8.2. For this path, $\nu_1 \approx 0.73961$. (b) The periodic orbit for the parameter values at the large dot near the label (a) in panel (a), in (u, v, w) space (top), and for w versus time (bottom).

propagation in pancreatic acinar cells. The model was originally developed in [34] and [35] and further studied in [33]:

$$\begin{aligned}
\dot{c} &= d \\
D_c \dot{d} &= sd - J \\
s \dot{c}_e &= \gamma(J_{\text{serca}} - (k_f P_{\text{IPR}} + \nu_1 P_{\text{YR}} + J_{\text{er}})(c_e - c)) \\
s \dot{R} &= \varphi_{-2} O - \varphi_2 p R + (k_{-1} + l_{-2}) I_1 - \varphi_1 R \\
s \dot{O} &= \varphi_2 p R - (\varphi_{-2} + \varphi_4 + \varphi_3) O + \varphi_{-4} A + k_{-3} S \\
s \dot{A} &= \varphi_4 O - (\varphi_{-4} + \varphi_5) A + (k_{-1} + l_{-2}) I_2 \\
s \dot{I}_1 &= \varphi_1 R - (k_{-1} + l_{-2}) I_1 \\
s \dot{I}_2 &= \varphi_5 A - (k_{-1} + l_{-2}) I_2 \\
s \dot{w} &= k_{\text{cm}}(w_\infty - w)/w_\infty.
\end{aligned} \tag{8.3}$$

Here c denotes the concentration of calcium ions in the cytoplasm, c_e gives the concentration of calcium ions in the endoplasmic reticulum, and the variables R , O , A , I_1 and I_2 denote the fraction of receptors in various states. The bifurcation parameters used are s (the wave speed) and p (the concentration of inositol trisphosphate in the cytoplasm). The definitions of the quantities J , J_{serca} etc. and the values of all constants used in the numerical computations using these equations are given in the Appendix.

As described in [4], a branch of E -homoclinic bifurcations is seen to fold many times (in a ‘homoclinic snake’) for $s \approx 6.7$ and p varying between about 1.88 and 2.63. Figure 8.6 shows various parts of the bifurcation diagram and some representative phase portraits for this phenomenon. A feature of this bifurcation diagram that we highlight is that turning points of the snake accumulate on six different values of p , which suggests that there are in fact six cyclically connected EP1t-points and associated turning points as in the case discussed in §7.1 and illustrated in Fig. 7.4.

AUTO is not reliable for finding Floquet multipliers in such a stiff system and hence it is hard to compare the theoretical predictions for the rate of convergence of the folds of E -homoclinics with what is seen in the numerical bifurcation set. Furthermore, our analysis is restricted to \mathbb{R}^3 and so may not apply to this example. However, the phenomenon seen in this system is qualitatively the same as predicted by our theory. There is extremely fast convergence of the turning points of the homoclinic snake (the different turning points on the E -homoclinic curve are numerically indistinguishable in the (p, s) -parameter space) which is consistent with our theory in the case that the system is stiff. The lack of reliable estimates of the Floquet multipliers prevents us from determining which case of the theory might be relevant to this system (i.e., positive Floquet multipliers or negative Floquet multipliers). The eigenvalues of the equilibrium can, however, be determined. At the left edge of the snaking envelope the eigenvalues are computed to be -4.32 , -3.82 , -2.01 , -0.131 , $-0.031 \pm 0.138i$, -0.0144 , -0.00673 , and 0.4352564 , while the eigenvalues at the right edge of the envelope are -5.24 , -4.48 , -2.13 , -0.137 , -0.0151 , -0.0922 , $-0.000577 \pm 0.1485265i$, and 0.3613053 . We note that the two leading eigenvalues for the left edge of the snaking envelope are real, and those for the right edge are complex, but this difference does not affect the analysis of the E -homoclinic bifurcations, as discussed in §5.

9. Conclusion. This paper has (partially) unfolded the dynamics occurring near an EP1t-point, i.e., near a codimension-two heteroclinic cycle connecting a hyperbolic equilibrium and a hyperbolic periodic orbit in the case that the connection from the

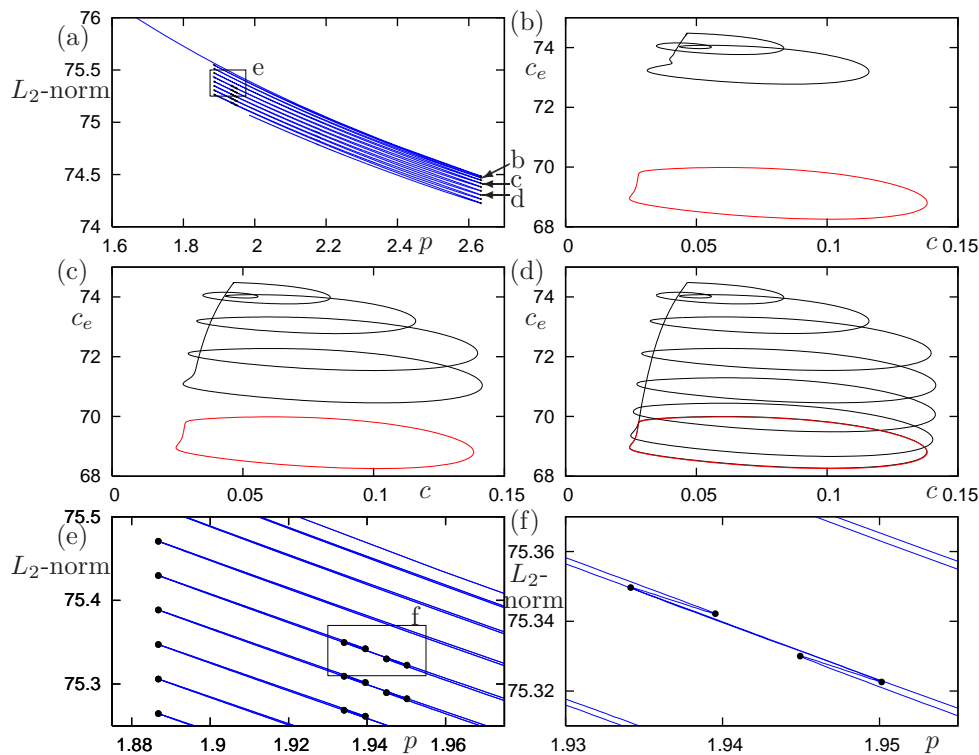


FIG. 8.6. Snaking diagram of E -homoclinic orbits in the nine-dimensional calcium dynamics model, equations (8.3). Panel (a) shows the location of all the turning points (black points) of E -homoclinic orbits in the parameter- vs - L_2 -norm plane. The homoclinic orbit and associated periodic orbit at turning points b , c , and d , near the right edge of the snaking envelope, are depicted in the corresponding panels (b)–(d). Panels (e) and (f) show two successive magnifications of panel (a) near a complex sequence of internal folds.

equilibrium to the periodic orbit is of codimension one and the connection from the periodic orbit to the equilibrium occurs at a tangency of the unstable manifold of the periodic orbit and the stable manifold of the equilibrium. We were initially motivated to perform this study as part of a wider project which aimed to categorise some of the ways in which branches of homoclinic orbits of equilibria can terminate near Hopf bifurcations in excitable systems [4]; EP1t-points turn out to be relevant in this context.

We have performed a geometric analysis that has enabled us to locate homoclinic bifurcations of the equilibrium, homoclinic tangencies of the periodic orbit, and folds of periodic orbits, all in a neighbourhood of an EP1t-point, and to deduce scaling laws for these bifurcations. Using simple geometric assumptions about the way in which two or more EP1t-points might be globally connected (in parameter space) we have shown why wide snaking curves of homoclinic bifurcations of the equilibrium are seen in some systems with EP1t-points. Our main results are summarised in §2 and illustrated with numerical examples in §8.

Our analysis has been via standard methods, i.e., the construction and analysis of geometric return maps valid in a neighbourhood of an EP1t-point. We have not given complete proofs of the validity of our model as an approximation to the dynamics

near the heteroclinic cycle, choosing to focus instead on providing a simple picture of the behaviour of the main codimension-one bifurcations that occur, but we believe that a rigorous proof is possible.

Our analysis has been restricted to \mathbb{R}^3 , the lowest possible phase space dimension in which an EP1t-point can occur. It seems likely that results such as the homoclinic centre manifold theorem and techniques such as Lin's method could be used to extend the results to higher dimensions, but we have not attempted to do so. However, we note that one of the numerical examples we considered was nine-dimensional, and the main results of our analysis seemed to apply to that example, lending credence to our view that the results in this paper will be valid beyond \mathbb{R}^3 .

We have performed only a partial unfolding of an EP1t-point. Aspects of the dynamics that remain to be investigated include the existence of period-doubling bifurcations of periodic orbits, the presence of chaotic dynamics, and bifurcations involving multi-pulse homoclinic orbits (passing more than once near the equilibrium). There are also other related cases that could be considered. For instance, analogous calculations could cast light upon the dynamics seen near codimension-two EP2 cycles such as those described in [28]. Lastly, in the context of excitable systems, from which our interest in EP1t-points arose, the homoclinic orbits of interest in our study actually correspond to isolated travelling pulses in the underlying partial differential equation models; it would be of interest to investigate any implications for pulse stability arising from the dynamics we have uncovered. All of these phenomena remain the subject for future work.

Acknowledgements: The authors acknowledge helpful conversations with Bernd Krauskopf, David Simpson, James Sneyd and Arnd Scheel. This work was supported in part by the New Zealand Institute of Mathematics and Its Applications, the Weierstrass Institute Berlin, the University of Auckland Research Committee, the UK Engineering and Physical Sciences Research Council, and the National Science Foundation grant DMS-0605238. J.R. acknowledges support from a PIMS fellowship, the SPP 1095 program of the German Research Foundation DFG, and the NDNS+ program of the Dutch Research Foundation NWO.

Appendix A. Quantities and constants for the calcium model equations.

In numerical computations using equations (8.3) the following quantities and constants were used:

$$J = (k_f P_{\text{IPR}} + \nu_1 P_{\text{rYR}} + J_{\text{er}})(c_e - c) - J_{\text{serca}} - J_{\text{mito}} + \delta(J_{\text{in}} - J_{\text{pm}})$$

$$\begin{aligned} K_a &= (k_{\text{am}}/k_{\text{ap}})^{\frac{1}{4}} & K_b &= (k_{\text{bm}}/k_{\text{bp}})^{\frac{1}{3}} & K_c &= k_{\text{cm}}/k_{\text{cp}} \\ l_{-2} &= l_2 k_{-1}/(k_1 L_1) & l_{-6} &= k_{-4} l_6/(k_4 L_5) & l_{-4} &= k_{-2} l_4/(k_2 L_3) \end{aligned}$$

$$\begin{aligned}
w_\infty &= \frac{1 + (K_a/c)^4 + (c/K_b)^3}{1 + 1/K_c + (K_a/c)^4 + (c/K_b)^3} & J_{\text{mito}} &= V_{\text{mito}} \frac{c^3}{1 + c^2} \\
P_{\text{Yr}} &= w \frac{1 + (c/K_b)^3}{1 + (K_a/c)^4 + (c/K_b)^3} & J_{\text{in}} &= J_{\text{inbase}} + 0.05p \\
S &= 1 - R - O - A - I_1 - I_2 & P_{\text{IPR}}(O, A) &= (O/10 + 9A/10)^4 \\
\varphi_1(c) &= \frac{(k_1 L_1 + l_2)c}{L_1 + c(1 + L_1/L_3)} & \varphi_2(c) &= \frac{k_2 L_3 + l_4 c}{L_3 + c(1 + L_3/L_1)} \\
\varphi_{-2}(c) &= \frac{k_{-2} + l_{-4}c}{1 + c/L_5} & \varphi_3(c) &= \frac{k_3 L_5}{L_5 + c} \\
\varphi_4(c) &= \frac{(k_4 L_5 + l_6)c}{L_5 + c} & \varphi_{-4}(c) &= \frac{L_1(k_{-4} + l_{-6})}{L_1 + c} \\
\varphi_5(c) &= \frac{(k_1 L_1 + l_2)c}{L_1 + c} & & \\
\Phi_2 &= \varphi_{-2}/\varphi_2 & \Phi_4 &= \varphi_{-4}/\varphi_4 \\
A &= pR/(p + \Phi_2\Phi_4 + p\Phi_4) & J_{\text{IPR}} &= k_f A^4 \\
J_{\text{pm}}(c) &= \frac{V_{\text{pm}}c^2}{K_{\text{pm}}^2 + c^2} & J_{\text{serca}}(c, c_e) &= \frac{V_{\text{serca}}c}{c_e(K_{\text{serca}} + c)}
\end{aligned}$$

J_{inbase}	J_{er}	γ	V_{serca}	K_{serca}	V_{pm}	K_{pm}	δ	D_c	ν_1	V_{mito}
0.2	0.002	5.405	120.0	0.18	28.0	0.425	0.1	20	0.04	0
k_f	k_{ap}	k_{am}	k_{bp}	k_{bm}	k_{cp}	k_{cm}	l_2	l_6	L_1	L_5
0.32	1500	28.8	1500	385.9	1.75	0.1	1.7	4707	0.12	54.7
l_4	L_3	k_1	k_{-1}	k_2	k_{-2}	k_3	k_{-3}	k_4	k_{-4}	
1.7	0.025	0.64	0.04	37.4	1.4	0.11	29.8	4	0.54	

REFERENCES

- [1] R. BAMÓN, R. LABARCA, R. MAÑÉ, and M.J. PACÍFICO, The explosion of singular cycles, *Inst. Hautes Études Sci. Publ. Math.*, 78 (1994), pp. 207–232.
- [2] M. BECK, J. KNOBLOCH, D.J.B. LLOYD, B. SANDSTEDE, and T. WAGENKNECHT, Snakes, ladders, and isolas of localised patterns, *SIAM J. Math. Anal.* (2009), in press.
- [3] A.R. CHAMPNEYS and V. KIRK, The entwined wiggling of homoclinic curves emerging from saddle-node/Hopf instabilities, *Physica D*, 195 (2004), pp. 77–105.
- [4] A.R. CHAMPNEYS, V. KIRK, E. KNOBLOCH, B.E. OLDEMAN and J. SNEYD, When Shil'nikov meets Hopf in excitable systems, *SIAM J. Dyn. Syst.*, 6 (2007), pp. 663–693.
- [5] S.-N. CHOW, B. DENG and B. FIEDLER, Homoclinic bifurcation at resonant eigenvalues, *J. Dyn. Diff. Eqns*, 2 (1990), pp. 177–244.
- [6] E.J. DOEDEL, AUTO-07P: Continuation and bifurcation software for ordinary differential equations, <http://cmvl.cs.concordia.ca/auto>
- [7] E.J. DOEDEL, B.W. KOOI, YU.A. KUZNETSOV and G.A.K. VAN VOORN, Continuation of connecting orbits in 3D-ODES: (I) Point-to-cycle connections, *Internat. J. Bifur. Chaos Appl. Sci. Engrg.* (2008), in press.
- [8] E.J. DOEDEL, B.W. KOOI, YU.A. KUZNETSOV and G.A.K. VAN VOORN, Continuation of connecting orbits in 3D-ODES: (II) Cycle-to-cycle connections, *Internat. J. Bifur. Chaos Appl. Sci. Engrg.* (2008), submitted.
- [9] A.C. FOWLER and C.T. SPARROW, Bifocal homoclinic orbits in four dimensions, *Nonlinearity*, 4 (1991), pp. 1159–1182.
- [10] P. GASPARD and X.-J. WANG, Homoclinic orbits and mixed-mode oscillations in far-from-equilibrium systems, *J. Stat. Phys.*, 48 (1987), pp. 151–199.

- [11] P. GASPARD, R. KAPRAL and G. NICOLIS, Bifurcation phenomena near homoclinic systems: A two-parameter analysis, *J. Stat. Phys.*, 35 (1984), pp. 697–727.
- [12] N.K. GAVRILOV and L.P. SHIL'NIKOV, On three-dimensional systems close to systems with a structurally unstable homoclinic curve, *Mat. USSR Sb.*, 17 (1972), pp. 467–485 & 19 (1973), pp. 139–156.
- [13] P.A. GLENDINNING and C. SPARROW, Local and global behavior near homoclinic orbits, *J. Stat. Phys.*, 35 (1984), pp. 645–696.
- [14] S.V. GONCHENKO, D.V. TURAEV, P. GASPARD and G. NICOLIS, Complexity in the bifurcation structure of homoclinic loops to a saddle-focus, *Nonlinearity*, 10 (1997), pp. 409–423.
- [15] J.K. HALE and X.-B. LIN, Heteroclinic orbits for retarded functional differential equations, *J. Diff. Eqns*, 65 (1986), pp. 175–202.
- [16] P. HIRSCHBERG and E. KNOBLOCH, The Shil'nikov-Hopf bifurcation, *Physica D*, 62 (1993), pp. 202–216.
- [17] A.J. HOMBURG and B. KRAUSKOPF, Resonant homoclinic flip bifurcations, *J. Dyn. Diff. Eqns*, 12 (2000), pp. 807–850.
- [18] M. KISAKA, H. KOKUBU and H. OKA, Bifurcations to N -homoclinic orbits and N -periodic orbits in vector fields, *J. Dyn. Diff. Eqns*, 5 (1993), pp. 305–357.
- [19] M. KISAKA, H. KOKUBU and H. OKA, Supplement to homoclinic-doubling bifurcation in vector fields, in R. BAMON, R. LABARCA, J. LEWOWICZ and J. PALIS, eds., *Dynamical Systems*, Longman, 1993, pp. 92–116.
- [20] B. KRAUSKOPF and B.E. OLDEMAN, Bifurcations of global reinjection orbits near a saddle-node Hopf bifurcation, *Nonlinearity*, 19 (2006), pp. 2149–2167.
- [21] B. KRAUSKOPF and T. RIESS, A Lin's method approach finding and continuing heteroclinic connections involving periodic orbits, *Nonlinearity*, 21 (2008), pp. 1655–1690.
- [22] Yu. A. KUZNETSOV, *Elements of Applied Bifurcation Theory* (third edition), Springer-Verlag, New York, 2004.
- [23] R. LABARCA, Bifurcation of contracting singular cycles, *Ann. Sci. École Norm. Sup.*, 28 (1995), pp. 705–745.
- [24] R. LABARCA and B. SAN MARTÍN, Prevalence of hyperbolicity for complex singular cycles, *Bol. Soc. Brasil. Mat. (N.S.)*, 28 (1997), pp. 343–362.
- [25] C.A. MORALES and M.J. PACÍFICO, Degenerated singular cycles of inclination-flip type, *Ann. Sci. École Norm. Sup.*, 31 (1998), pp. 1–16.
- [26] M.J. PACÍFICO and A. ROVELLA, Unfolding contracting singular cycles, *Ann. Sci. École Norm. Sup.*, 26 (1993), pp. 691–700.
- [27] J. PALIS and F. TAKENS, *Hyperbolicity and Sensitive Chaotic Dynamics at Homoclinic Bifurcations*, Cambridge Stud. Adv. Math., vol. 35, Cambridge University Press, Cambridge, 1993.
- [28] J.D.M. RADEMACHER, Homoclinic orbits near heteroclinic cycles with one equilibrium and one periodic orbit, *J. Diff. Eqns*, 218 (2005), pp. 390–443.
- [29] J.D.M. RADEMACHER, Lyapunov-Schmidt reduction for unfolding heteroclinic networks of equilibria and periodic orbits with tangencies, preprint, <http://homepages.cwi.nl/~rademach/linper.pdf>
- [30] T. RIESS, A Lin's method approach to heteroclinic cycles involving periodic orbits - analysis and numerics, PhD thesis, University of Ilmenau (2008).
- [31] B. SANDSTEDTE, *Verzweigungstheorie homokliner Verdopplungen*, Thesis, University of Stuttgart (1993), <http://www.dam.brown.edu/people/sandsted/publications.php?type=theses>
- [32] B. SANDSTEDTE, Center manifolds for homoclinic solutions, *J. Dyn. Diff. Eqns*, 12, (2000), pp. 449–510.
- [33] D. SIMPSON, V. KIRK and J. SNEYD, Complex oscillations and waves of calcium in pancreatic acinar cells, *Physica D*, 200 (2005), pp. 303–324.
- [34] J. SNEYD and J.F. DUFOUR, A dynamic model of the type-2 inositol trisphosphate receptor, *Proc. Natl. Acad. Sci. USA*, 99 (2002), pp. 2398–2403.
- [35] J. SNEYD, K. TSANEVA-ATANASOVA, J.I.E. BRUCE, S.V. STRAUB, D.R. GIOVANNUCCI and D.I. YULE, A model of calcium waves in pancreatic and parotid acinar cells, *Biophys. J.*, 85 (2003), pp. 1392–1405.
- [36] S. STERNBERG, On the structure of local homeomorphisms of Euclidean n -space, II, *Am. J. Math.*, 80 (1958), pp. 623–631
- [37] D.V. TURAEV, On dimension of non-local bifurcational problems, *Internat. J. Bifur. Chaos Appl. Sci. Engrg.*, 6 (1996), pp. 919–948.